Geochemistry, Geophysics, Geosystems®

AGU ADVANCING EARTH AND SPACE SCIENCE

RESEARCH ARTICLE
10.1029/2022GC010517

Key Points:

- We image seismic velocity interfaces beneath the state of Alaska using common conversion point stacking of Sp converted phases
- The Moho, the lithosphere-asthenosphere boundary, and the base of a low velocity asthenospheric layer are resolved
- The low asthenospheric velocities are consistent with the widespread presence of partial melt

Supporting Information:

Supporting Information may be found in the online version of this article.

Correspondence to:

I. Gama,
isabellagamad@gmail.com

Citation:

Gama, I., Fischer, K. M., & Hua, J. (2022). Mapping the lithosphere and asthenosphere beneath Alaska with Sp converted waves. *Geochemistry, Geophysics, Geosystems*, *23*, e2022GC010517. https://doi.org/10.1029/2022GC010517

Received 12 MAY 2022
Accepted 24 AUG 2022

Author Contributions:

Conceptualization: Isabella Gama, Karen M. Fischer
Data curation: Isabella Gama
Formal analysis: Isabella Gama
Funding acquisition: Karen M. Fischer
Investigation: Isabella Gama
Methodology: Isabella Gama, Karen M. Fischer, Junlin Hua
Project Administration: Karen M. Fischer
Resources: Isabella Gama, Karen M. Fischer, Junlin Hua
Software: Isabella Gama, Junlin Hua
Supervision: Karen M. Fischer

Mapping the Lithosphere and Asthenosphere Beneath Alaska With Sp Converted Waves

Isabella Gama[1], Karen M. Fischer[1], and Junlin Hua[1,2]

[1]Department of Earth, Environmental and Planetary Sciences, Brown University, Providence, RI, USA, [2]Jackson School of Geosciences, University of Texas at Austin, Austin, TX, USA

Abstract We obtained a 3D image of crust and mantle seismic velocity gradients beneath the state of Alaska using common-conversion point (CCP) stacking of S-to-p converted body waves recorded by hundreds of stations from the NSF EarthScope Transportable Array and other portable arrays and permanent networks. Moho depths delineate the thick crust of the underthrust Yakutat terrane and the crustal root beneath the Brooks Range. The North American lithosphere is particularly thin close to the subducting lithosphere in the Alaska subduction zone, consistent with thinning of the upper plate by subduction zone flow and melt rising from the mantle wedge. The lithosphere remains relatively thin far to the northwest and north, including the Seward Peninsula and regions to the south of the Brooks Range where lithospheric extension and foundering may have played a role. The lithosphere dramatically thickens beneath the Brooks Range and northern Arctic Alaska terrane where it appears to be both cold and highly viscous. The CCP stack also revealed a pronounced positive velocity gradient at depths of 130–230 km that represents the base of a layer within the asthenosphere whose low velocities are best explained by the presence of partial melt. Although this gradient is present close to the subducting lithosphere, where partial melting is enabled by slab-derived fluids, it is strongest beneath the Seward Peninsula and northeast of the Wrangell volcanic field, suggesting the presence of partial melt in the asthenosphere hundreds of kilometers away from the slab, likely due to decompression melting in upwelling asthenosphere.

Plain Language Summary We used recordings of distant earthquakes at hundreds of seismic stations to create a 3D image of the crust and mantle beneath the state of Alaska. We measured the thicknesses of the crust and the lithosphere, and the depth of a mantle feature that we interpreted as the base of a layer containing partial melt. The crust is particularly thick beneath the Brooks Range in the north, and where the plate subducting in the south is carrying the crust of the Yakutat terrane beneath the upper plate. The upper plate appears to have been thinned by subduction zone flow and partial melt rising from the mantle wedge in central Alaska, and it is much thicker in the far north. Above depths of 130–230 km, partial melt exists near the subducting plate, where slab-derived fluids allow melting of mantle rocks. However, the effects of partial melt are largest beneath the Seward Peninsula and northeast of the Wrangell volcanic field, hundreds of kilometers away from the slab, where melting is enabled by rising mantle.

1. Introduction

The global distribution of partial melt in the asthenosphere is still widely debated. In subduction zones, seismic velocity and attenuation models have been used to trace the generation and transport of partial melt in the mantle wedge from just above the subducting slab to the arc (e.g., Abers et al., 2014; Syracuse et al., 2008; Tamura, 2003), including in Alaska (Eberhart-Phillips et al., 2006; McNamara & Pasyanos. 2002; Soto Casteneda et al., 2021), and beneath back-arc spreading centers (e.g., Wei & Wiens, 2018, 2020). However, the distribution of partial melt on a more widespread basis in subduction zone mantle wedges, and its extent beneath adjacent lithosphere, remains uncertain.

Mantle seismic velocity discontinuities—or vertically localized seismic velocity gradients—have potential to help resolve the distribution of melt in the mantle. A negative velocity gradient (decreasing velocity with depth) at the lithosphere-asthenosphere boundary (or LAB) has been explained by a variety of models. While temperature clearly plays a role in creating high seismic velocities in the mantle lithosphere (Hirth & Kohlstedt, 2003; Stixrude & Lithgow-Bertelloni, 2005) additional factors have been invoked to produce negative velocity gradients that are vertically localized, including the presence of volatiles and partial melt in the asthenosphere, elastically

Validation: Isabella Gama
Visualization: Isabella Gama
Writing – original draft: Isabella Gama
Writing – review & editing: Isabella Gama, Karen M. Fischer

accommodated grain boundary sliding, near-solidus weakening, and seismic anisotropy (e.g., L. N. Hansen et al., 2016; Yamauchi & Takei, 2020; also see reviews in Fischer et al., 2020; Karato & Park, 2018; Rychert et al., 2018a, 2018b). In some regions the seismic LAB has been associated with solidi, for example, a relatively dry peridotite solidus in the western U.S. (Golos & Fischer, 2022; Plank & Forsyth, 2016), a hydrated peridotite solidus in subduction zones (e.g., Wang et al., 2020), or a carbonated peridotite solidus beneath the oceans and in subduction zones (e.g., Dasgupta, 2018; Hammouda et al., 2021; Hirschmann, 2010). In Alaska, Rondenay et al. (2010) imaged a negative velocity gradient at depths of ∼60 km which they attributed to partial melt pooled beneath the base of the North American lithosphere. Mantle discontinuities may also be created at the lower boundaries of the layers where asthenospheric temperatures exceed the temperature of a particular solidus (e.g., Dasgupta, 2018; Hammouda et al., 2021; Hirschmann, 2010; Wang et al., 2020), creating a positive velocity gradient (PVG) with depth, as has been observed beneath a number of regions (Hua, Fischer, Wu, & Blom, 2020; Miller et al., 2015; Rychert et al., 2013, 2018a, 2018b; Wu et al., 2021). The presence of a small amount of partial melt has also been invoked to explain zones of high electrical conductivity in some regions of the asthenosphere (e.g., Chesley et al., 2019; Naif et al., 2013; Selway et al., 2019).

Converted body waves (such as Sp and Ps) and reflected phases are effective at imaging vertically localized velocity gradients and provide an important complement to body and surface wave tomography which reflect velocities or velocity anomalies throughout a given volume. For example, the addition of Sp (e.g., Gama et al., 2021), Ps (e.g., Berg et al., 2020; Bodin et al., 2013; Calo et al., 2016; Julia et al., 2000; Martin-Short et al., 2018; Porritt et al., 2015; Roy & Romanowicz, 2017; Schmandt et al., 2015; Shen & Ritzwoller, 2016; Shen et al., 2013, 2018; Ward & Lin, 2018), or Sp and Ps phases (Eilon et al., 2018) to inversions of surface wave phase velocities enhances vertical resolution of both mantle and Moho velocity gradients. Sp phases have an advantage over Ps in that Sp mantle arrivals are not over-printed by Moho reverberations, and Moho phases are not over-printed by reverberations from shallow crustal layers. Due to their Fresnel zones (e.g., Hansen & Schmandt, 2017; Mancinelli & Fischer, 2017) Sp phases are typically not able to accurately capture velocity gradients with dips of more than 10°–15° (e.g., Hansen & Schmandt, 2017; Hua, Fischer, Mancinelli, & Bao, 2020; Lekić & Fischer, 2017). However, Sp Fresnel zones are especially well-suited to imaging near-horizontal velocity gradients and for stacking approaches that rely on horizontal averaging, such as common conversion point (CCP) stacking (e.g., Hua, Fischer, Mancinelli, & Bao, 2020; Hua, Fischer, Wu, & Blom, 2020).

In this paper, we employed CCP stacking of Sp converted phases to study lithospheric and asthenospheric properties near the subduction zone and across the continental lithosphere beneath the state of Alaska. Prior studies have imaged mantle discontinuities beneath Alaska using Sp (Bauer et al., 2014; O'Driscoll & Miller, 2015) and Ps (Bauer et al., 2014; Chuang et al., 2017; Mann et al., 2022; Rondenay et al., 2008, 2010) phases; explored upper and subducting plate crustal structure with Ps data (Allam et al., 2017; Brennan et al., 2011; Ferris et al., 2003; Kim et al., 2014; Miller & Moresi, 2018; Miller et al., 2018; Rondenay et al., 2008, 2010; Veenstra et al., 2006; Zhang et al., 2019); and incorporated Sp (Gama et al., 2021) or Ps (Berg et al., 2020; Feng, 2021; Martin-Short et al., 2018; Ward & Lin, 2018) data in joint inversions with surface waves. However, to our knowledge this is the first study to comprehensively map crust and mantle discontinuities in Alaska with Sp phases recorded by the U.S. National Science Foundation (NSF) EarthScope Transportable Array (TA). In Alaska, the contrast between the active convergent margin in the south and the more stable continental region in the north (e.g., Finzel et al., 2015) provides insight on how asthenospheric signatures vary as a function of tectonic setting. We focused on three main boundaries: the crust—mantle boundary (or Moho) which is key for understanding the interaction of Alaskan tectonic terranes, the LAB, and the base of a low velocity asthenosphere layer which appears as a PVG. We argue for the presence of partial melt where the LAB and PVG are strong in some areas of Alaska and explore different mechanisms for melt generation and their variation beneath Alaska.

2. Data and Method

To image shear-wave velocity gradients, we applied CCP stacking to Sp phases from teleseismic earthquakes recorded by permanent and temporary broadband stations in Alaska, in particular the stations of the NSF EarthScope TA (Figure 1a). These data create a dense distribution of ray paths beneath Alaska; 20,210 Sp receiver functions were used to construct the 3D CCP volume. Each step of the data analysis process is described in the following sections.

10.1029/2022GC010517

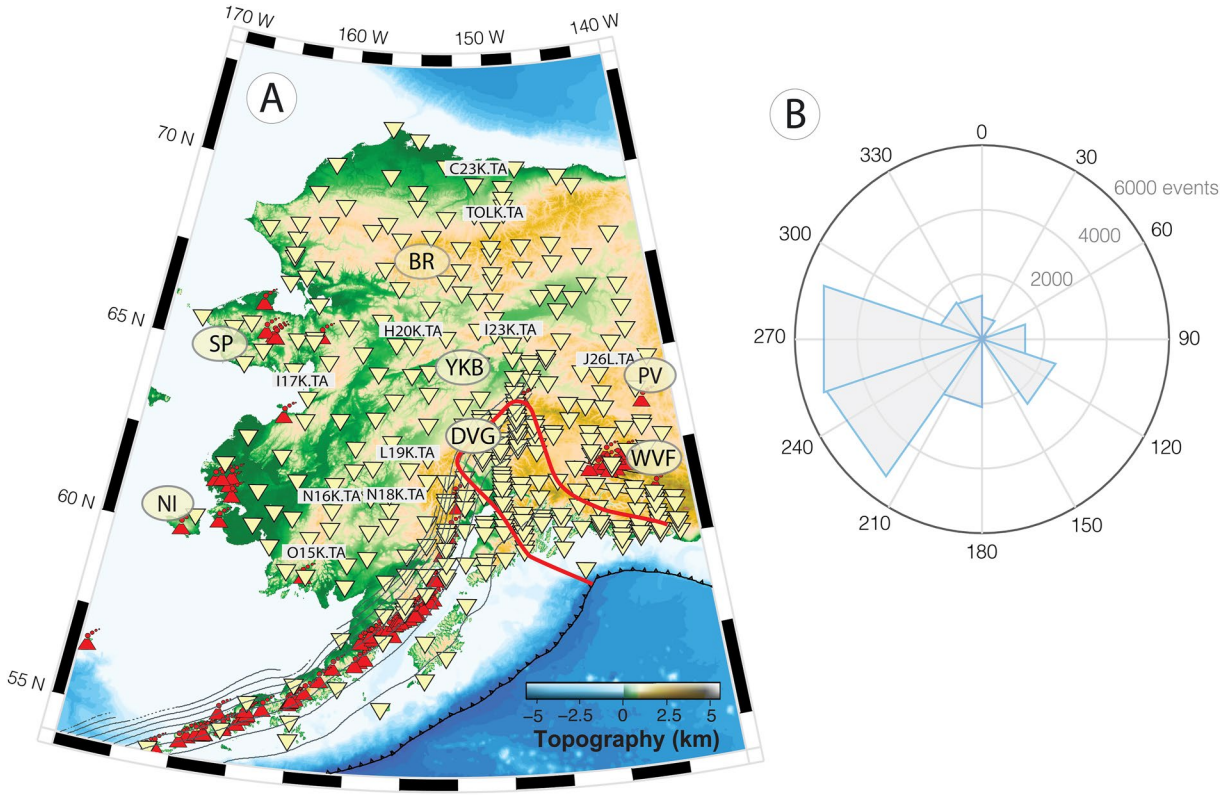

Figure 1. (a) Topographic map of Alaska (ETOPO1, Amante & Eakins, 2009) with the 449 stations used in the Sp common conversion point (CCP) stacks in yellow upside-down triangles. Red triangles show volcanoes (avo.alaska.edu) and gray lines are slab contours (Hayes et al., 2018). The red outline marks the extent of the Yakutat terrane (Eberhart-Phillips et al., 2006). Labeled stations indicate the location of the single stack stations in Figure 2. SP—Seward Peninsula; BR—Brooks Range; WVF—Wrangell Volcanic Field; DVG—Denali Volcanic Gap; YKB—Yukon-Koyukuk basin; NI—Nunivak Island; and PV—Prindle Volcano. (b) Distribution of earthquake back azimuths in the CCP stack.

2.1. Data

We selected earthquakes between the years of 1986 and 2021 and with Mw larger than 5.8. Epicentral distances of 50°–90° were used for Sp receiver functions and CCP stacking, and these paths are dominated by two back-azimuthal groups: 215°–255° (southeast Pacific events) and 255°–285° (north and northwest Pacific events) (Figure 1b). P waves used in calculating free-surface velocities were collected from events at 35°–90°.

We employed data from 449 seismic stations in Alaska (Figure 1a). Of these, 153 are EarthScope TA stations, and the remaining are other temporary and permanent stations. References for the relevant network codes (AK, AT, AV, DW, II, IM, IU, PN, PP, TA, US, XE, XR, XZ, YE, YG, YM, YV, and Z5) appear in the Acknowledgments.

2.2. Calculating Receiver Functions

To enable robust phase identification, we calculated the arrival time of P and S phases using an array-based method (Lekić & Fischer, 2014). We filtered the seismograms using a 2–100 s band-pass filter, and to separate waveforms into P and SV components, we used a free-surface transform (Kennett, 1991). We obtained the free-surface velocities needed for the free-surface transform using the particle motion modeling approach from Hua, Fischer, Wu, and Blom (2020) applied to direct P and S arrivals.

To calculate the Sp receiver functions, we deconvolved the SV component of the direct S arrival from the P component using a time-domain deconvolution method (Ligorría & Ammon, 1999). The resulting impulse responses were convolved with a Gaussian whose half-width is 0.9 s. To migrate the receiver functions to depth, we used the 3D velocity model from Nayak et al. (2020).

2.3. Quality Control

To ensure that very noisy and/or physically implausible receiver functions were not included in the CCP stack, we removed individual receiver functions that did not pass quality control tests for overall amplitude levels and for the presence of a Moho phase.

Two criteria were based on comparisons of the observed receiver function amplitudes relative to synthetic receiver function amplitudes predicted by the Nayak et al. (2020) velocity model for Alaska. However, we stress that the permitted ranges of receiver function amplitudes are broad enough that the choice of reference velocity model has almost no impact on the selected receiver functions. As long as Moho depths are consistent to within approximately ±10 km, a very wide range of reference models would yield similar results. Following the approach in Hua, Fischer, Wu, and Blom (2020), we generated synthetic receiver functions for 1D velocity models based on Nayak et al. (2020) at 1° horizontal increments, using the propagator matrix method (Keith & Crampin, 1977) and S wave ray parameters that are consistent with the observed receiver functions. From the predicted receiver functions for the entire region, for each depth we found the mean synthetic amplitude value, forming the vector $\mathbf{RF}_{\mathbf{mean}}$, and the half-width (half the range between minimum and maximum amplitudes, $\mathbf{RF}_{\mathbf{hw}}$). We discarded observed receiver functions ($\mathbf{RF}_{\mathbf{o}}$) with abnormally large amplitudes, identified by $\|\mathbf{RF}_{\mathbf{o}} - \mathbf{RF}_{\mathbf{mean}}\|^2_2$ greater than five times the median $\|\mathbf{RF}_{\mathbf{o}} - \mathbf{RF}_{\mathbf{mean}}\|^2_2$ from all receiver functions. This step removes 51% of the initial individual receiver functions. We also counted depth layers greater than 60 km where the receiver function amplitude $\mathbf{RF}_{\mathbf{o}}$ is either smaller than $\mathbf{RF}_{\mathbf{mean}} - \mathbf{0.8RF}_{\mathbf{hw}}$ or larger than $\mathbf{RF}_{\mathbf{mean}} + \mathbf{0.8RF}_{\mathbf{hw}}$. To remove sustained large amplitudes in the mantle, we removed observed receiver functions whose depth layer count was greater than the median from all observed receiver functions.

Given that clear Moho phases are observed across Alaska (e.g., Mann et al., 2022; Miller et al., 2018; Ward & Lin, 2018; Zhang et al., 2019), we also required that observed receiver functions have a positive amplitude in the potential Moho depth range of 15–60 km depth, and among these we discarded receiver functions with positive amplitudes smaller than 20% of the median amplitude from all receiver functions. We also discarded receiver functions with negative phases in the 15–60 km depth range that are three times larger than the median amplitude from all receiver functions in the 15–60 km depth range.

The 20,210 Sp receiver functions that remained after the quality control criteria were applied represent 30% of the individual receiver functions calculated from all collected waveforms. The effects of the quality control criteria are shown in stacks at single stations in Figure S1. Many features of the receiver functions with and without these thresholds are similar, although the thresholds typically result in higher amplitude Moho phases (positive amplitudes in the 20–55 km depth range), and, in some cases, clearer phases associated with negative velocity gradients (negative amplitudes) in the shallow mantle.

Other examples of observed receiver functions stacked at single stations are shown in Figure 2. Clear phases corresponding to positive velocity gradients at the Moho are observed at all stations. Stations in central and southern Alaska (H20K, I23K, I17K, J26L, L19K, N18K, N16K, and O15K) show phases consistent with negative velocity gradients in the 50–100 km depth range, whereas the two stations in the northern Arctic Alaska terrane (TOLK and C23K) have weaker and deeper negative phases in the potential LAB depth range.

2.4. CCP Stacking

To map individual Sp receiver functions to 3D space, we employed CCP stacking. For the source-receiver pair represent by each receiver function, P-wave raypaths were traced backward from the station through the grid of CCP points. For each layer of points in depth, the amplitude at the time in a receiver function that corresponds to that depth was added to the stack for a given grid point using a horizontal spatial weighting function. In contrast to prior studies that employed geographic bins of conversion points or weighting functions that reflect the Fresnel zones of vertically incident waves (e.g., Dueker & Sheehan, 1997; Kind et al., 2013; Lekić & Fischer, 2017), in this study we incorporated the properties of Sp sensitivity kernels at the true ray parameter of the incident S wave (Hansen & Schmandt, 2017; Hua, Fischer, Mancinelli, & Bao, 2020; Mancinelli & Fischer, 2017), using the spatial weighting functions developed by Hua, Fischer, Wu, and Blom (2020). The standard deviation of the stacked receiver function amplitude was used to quantify uncertainty in the CCP stacks. We applied a theoretical expression developed by Hua, Fischer, Wu, and Blom (2020) for precisely estimating the standard deviation of any weighted average, eliminating the requirement for bootstrapping.

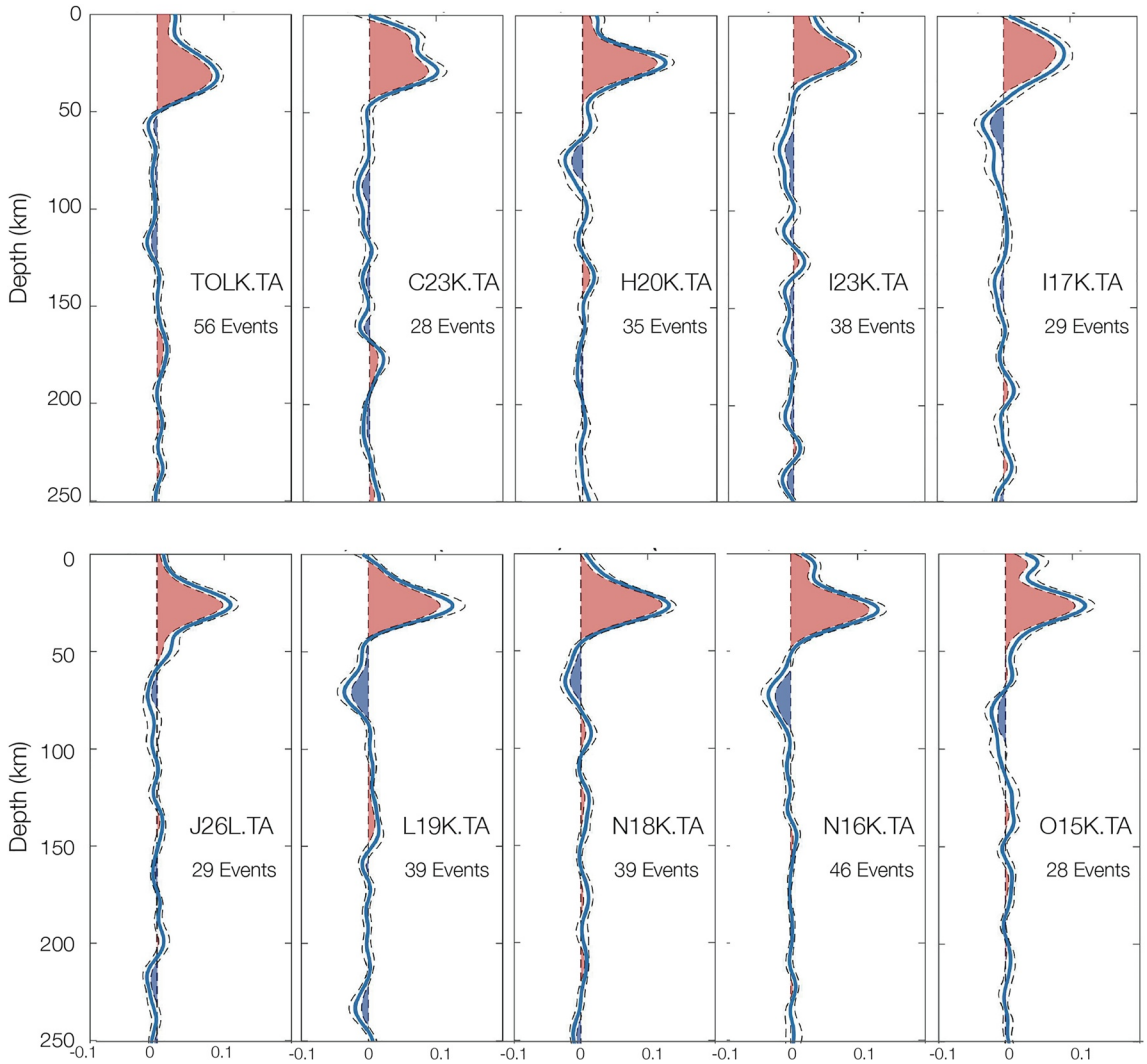

Figure 2. Single station stacks of Sp receiver functions (with Moho criteria) for select Transportable Array stations. Stacks were calculated using earthquakes from all back azimuths. Station locations are shown in Figure 1. Red phases correspond to velocity increases with depth and blue to velocity decreases with depth. Sp polarities have been flipped to match the Ps convention.

3. Results

In the CCP stack, we found three primary velocity gradients: (a) the Moho in the 15–66 km depth range, (b) a negative velocity gradient that can be interpreted as the LAB largely in the 50–170 km depth range, and (c) a deeper PVG in the mantle in the 130–230 km depth range (hereafter called the PVGm). These features and the CCP stacks in general are shown in: a map of the summed CCP weights for all receiver functions in the stack at a depth of 200 km, also with profile locations (Figure 3), profiles with depth (Figures 4–6) and in maps of velocity gradient depths and amplitudes (Figures 7–9). In the stacks, positive velocity gradients at the Moho or in the mantle are in red, and the stronger phases in blue represent a significant decrease in velocity, such as the LAB.

To ensure that we interpreted the CCP stack only where the observed phases are robust, we defined cutoff criteria for interpretation based on sampling and stack standard deviation. We ignored regions of the stack with low sampling based on their relative weight values (values of less 0.1 and 0.05 for the PVGm and the LAB, respectively) or where the amplitude value did not exceed two times its standard deviation. We also ignored small amplitude variations, those below an amplitude cutoff of 0.003. To measure the depths of the Moho and PVGm, we applied the phase picking algorithm from Hua et al. (2018), using additional criteria from Hua, Fischer, Wu, and Blom (2020), to positive amplitudes within the depth window for each feature (10–70 km for the Moho and

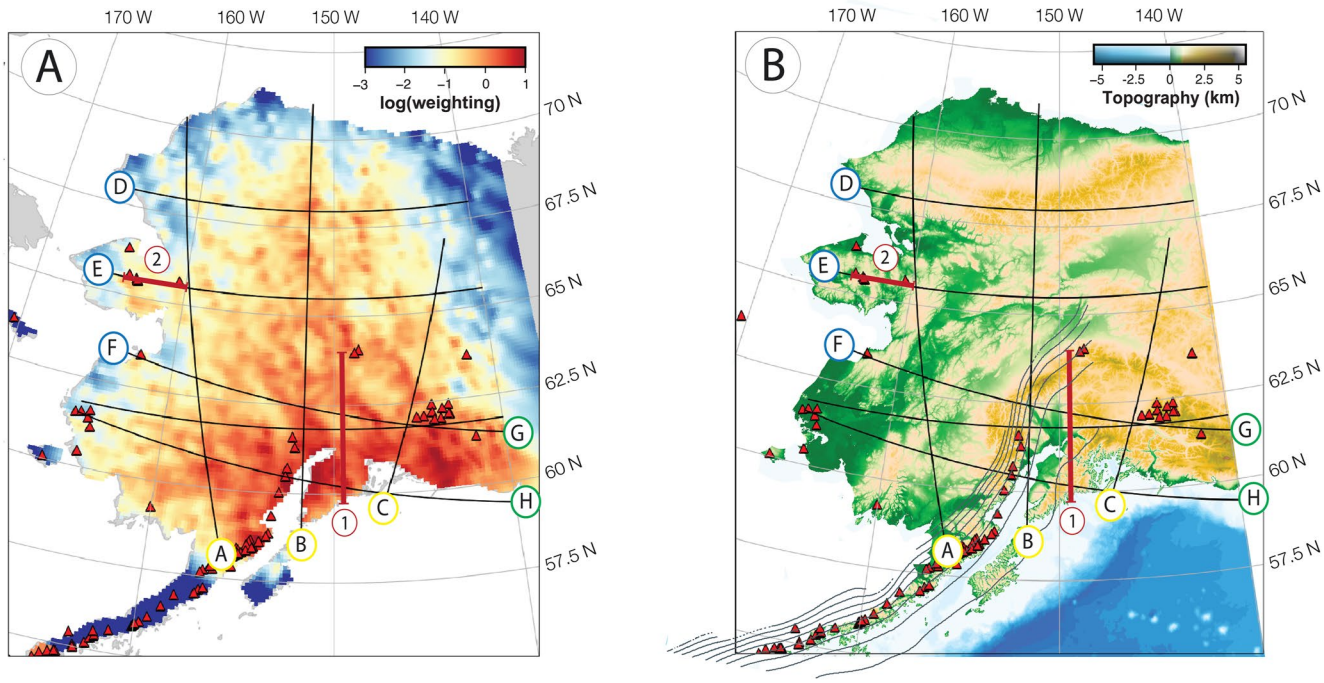

Figure 3. Maps of locations of cross-sections through the common conversion point stack shown on backgrounds of (a) summed weighting functions. Darker red on the weighting map shows areas of higher weighting, approximately corresponding to a greater density of Sp paths. (b) Topographic map of Alaska with volcanoes in red. Both panels show profiles in Figures 4–6.

100–250 km for the PVGm). This approach treats the CCP stack amplitudes as a probability distribution, where larger amplitudes correspond to higher probabilities, the expected depth from the probability distribution is associated with the center depth of the velocity gradient, and one standard deviation of the distribution characterizes the uncertainties in depth. LAB depths were chosen in a similar manner, except using negative amplitudes in the 40–200 km depth range. We retained only those picked phase depths that are continuous within a 0.5° radius. Examples of depth picks are shown in Figure 6, with Moho picks in profile 1, and LAB and PVGm picks in profile 2. Across most of these profiles, the phases are picked near the apparent center of the band of the most positive (Moho and PVGm) or negative (LAB) amplitudes. However, in some cases the probability distribution contains multiple peaks in distinct depth ranges (e.g., the four most western LAB picks in profile 2) and the resulting expected depth falls between the peaks, as would be expected if all were part of the same velocity gradient. In other cases, the presence of multiple peaks causes an increase in the standard deviation of the picked depth, as shown for the PVGm picks in profile 2 at longitudes of −160 to −161°E. Gaps in the picking typically reflect low amplitudes, as in the case of the LAB phase near −160°E.

3.1. Crust-Mantle Boundary

Profiles through the CCP stack show the crust is thickest beneath the Brooks Range in northern Alaska (Figure 4, profiles A and B) and where Yakutat crust is underthrust beneath North American crust in the south (Figure 4, profiles B and F; Figure 5, profiles C, G, and H). In the latter case, the underthrust Yakutat terrane is connected to the seismicity of the subducting lithosphere (e.g., Figure 4, profile C and Figure 5, profiles G and H). Where the Yakutat crust is underthrust beneath the North American crust, the picking algorithm typically selected the larger amplitude of the two Mohos (e.g., profile 1 in Figure 6) in the 10–70 km depth range, unless the peaks were very similar in amplitude and then the pick lies between them. In some cases, a relatively clear Moho phase continues below depths of 70 km (e.g., Figure 5, profiles G and H; Figure 6, profile 1) but at these depths the subducting lithosphere is no longer in contact with the upper plate, and we do not use these deeper portions of the subducting Moho in the Moho picks shown in Figure 7. Moho picks were retained only where the depth of the pick lies more than 5 km beneath the first non-zero amplitude in the stack at that latitude and longitude. Some of the profiles with the underthrust Yakutat crust also show negative energy at the interface between the North American and

10.1029/2022GC010517

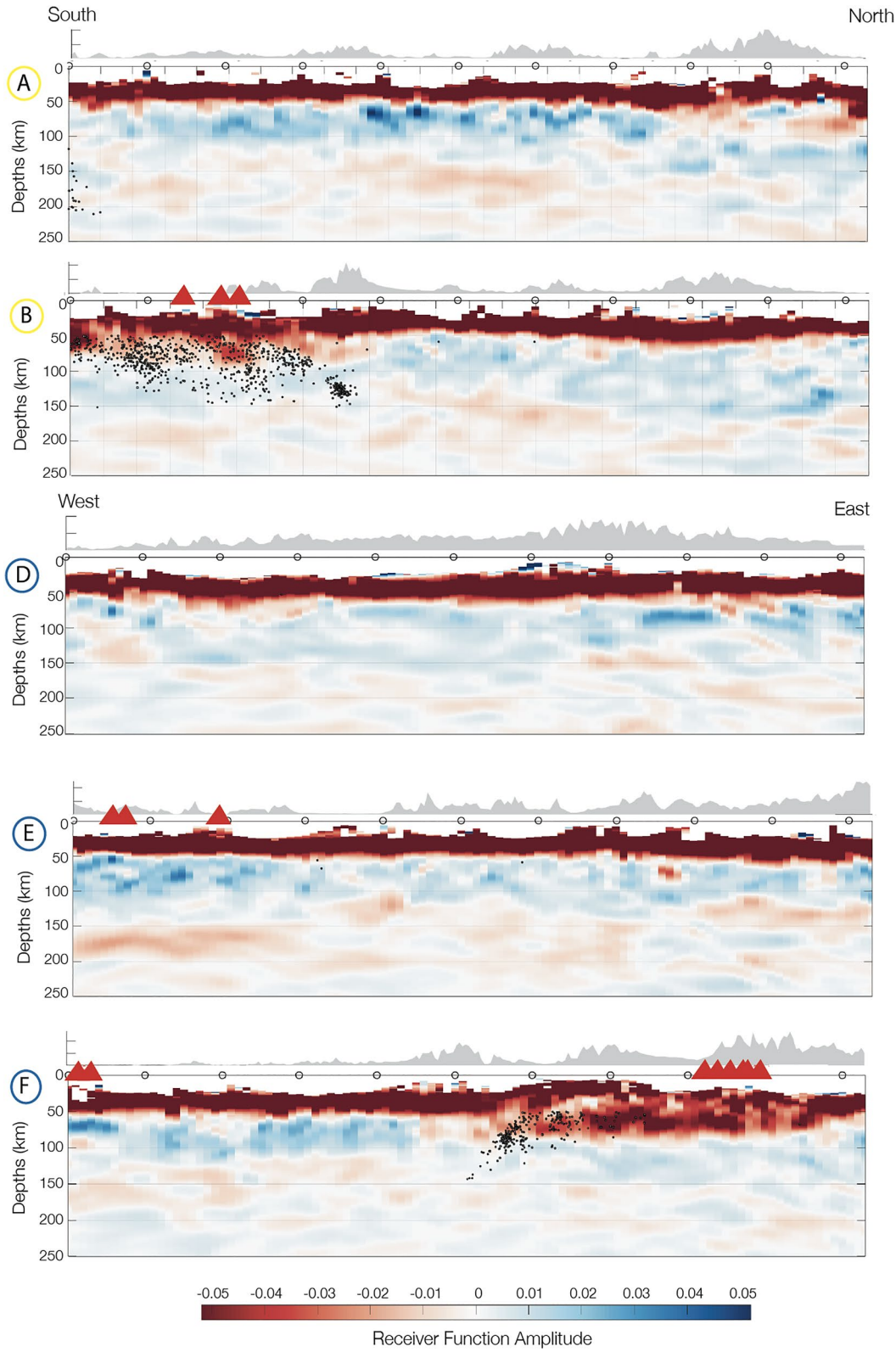

Figure 4. Profiles through the common conversion point stack. Red amplitudes correspond to increasing velocity with depth and blue to decreasing velocity with depth. Profile locations are shown in Figure 3. Gray shading at the top shows topography (Amante & Eakins, 2009). Small black dots are earthquakes (ANSS Comprehensive Earthquake Catalog USGS) and red triangles are volcanoes within 50 km from the profile. White circles at the top mark distance along the profile as shown in Figure 3.

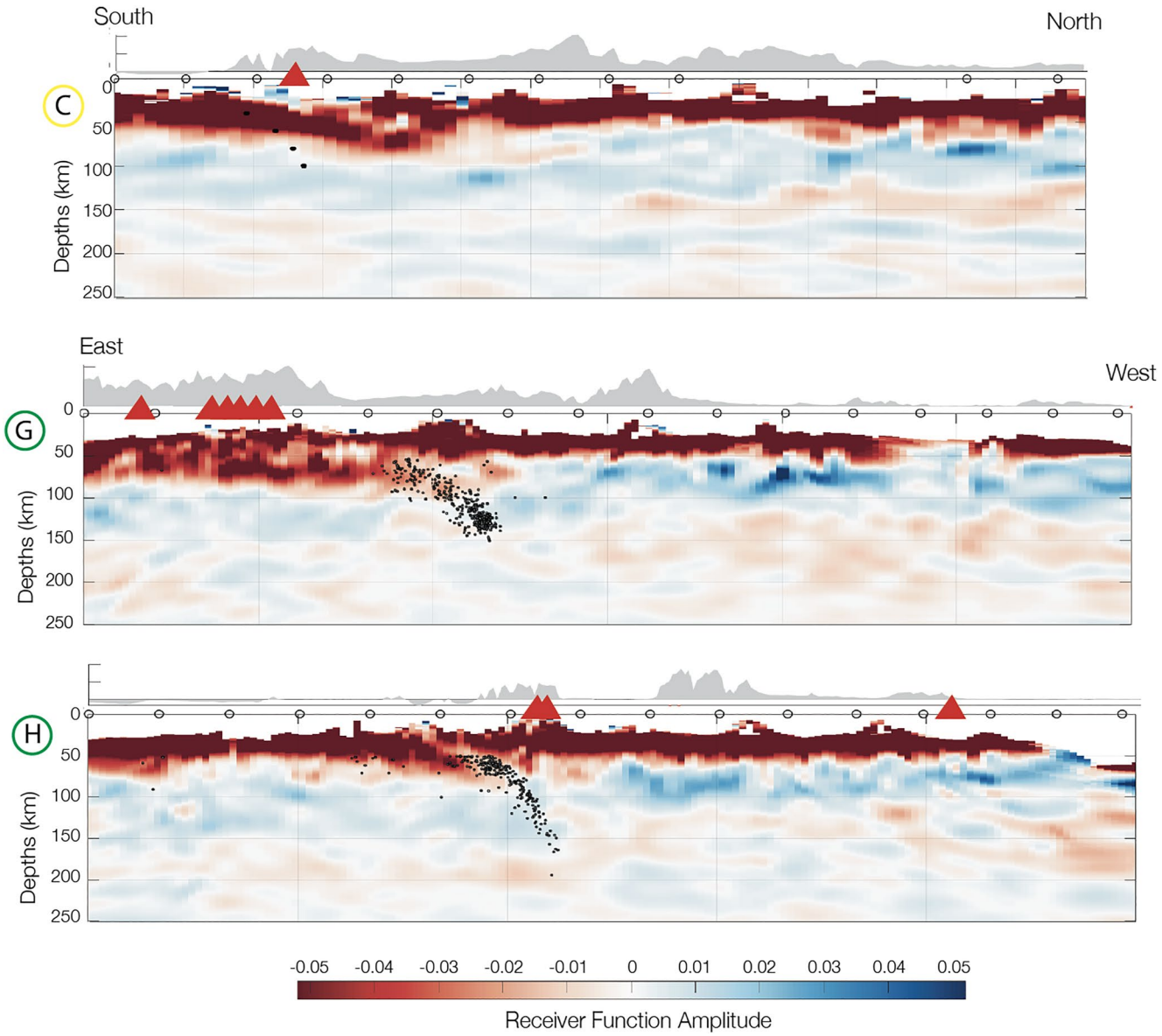

Figure 5. Profiles through the common conversion point (CCP) stack. Red amplitudes correspond to increasing velocity with depth and blue to decreasing velocity with depth. Profile locations are shown in Figure 3. Gray shading at the top shows topography (Amante & Eakins, 2009). Small black dots are earthquakes (ANSS Comprehensive Earthquake Catalog USGS) and red triangles are volcanoes within 50 km from the profile. The slab contours in profile C are from Daly et al. (2021). White circles at the top mark distance along the profile as shown in Figure 3. In profile H, note that the (blue) lithosphere-asthenosphere boundary phase from the base of the subducting plate continues all the way to the dipping seismicity, which does not make physical sense. This feature reflects the tendency of CCP stacking to horizontally smooth discontinuity signals (e.g., Hua, Fischer, Mancinelli, & Bao, 2020).

Yakutat Mohos (e.g., Figure 4, profile F and Figure 5, profiles G and H). This interface has also been observed in other studies (e.g., Fuis et al., 2008; Mann et al., 2022) with higher resolution than is possible in this CCP stack, where the data have been filtered with a 2–100 s bandpass.

Moho depths picked from the CCP stack range from 15 to 66 km (Figure 7). Their patterns north of the Denali fault are broadly consistent with previous studies (e.g., Haney et al., 2020; Miller et al., 2018; Ward & Lin, 2018; Zhang et al., 2019) where they overlap, although the maximum Moho depths from the CCP stack exceed those in Miller et al. (2018) and Zhang et al. (2019). However, south of the Denali fault, where positive velocity gradients associated with both Yakutat and North American Mohos exist, greater variations between studies occur, likely due to different choices in identifying a Moho arrival (e.g., Allam et al., 2017; Mann et al., 2022; Miller et al., 2018; Zhang et al., 2019). Overall, Moho depth estimates from the CCP stack extend farther and/or more

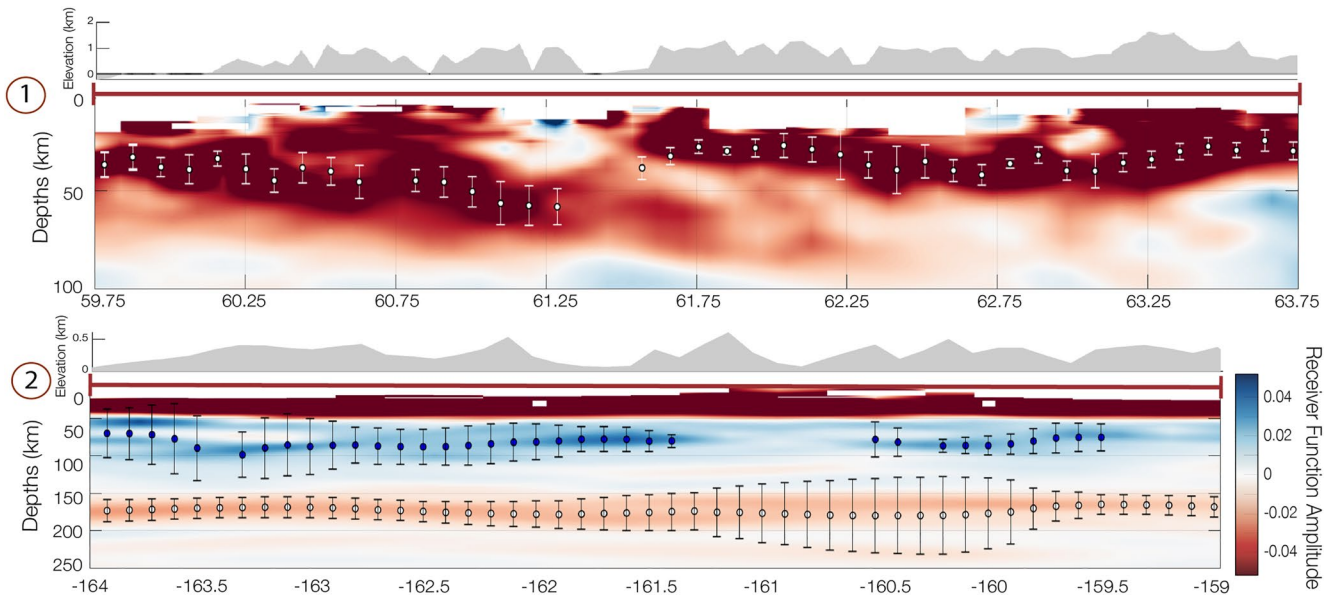

Figure 6. (upper) Examples of Moho depth picks (white dots with one standard deviation uncertainties) on profile 1; vertical axis from 0 to 100 km depth. (lower) Examples of lithosphere-asthenosphere boundary depth picks (blue dots) and positive velocity gradient depth picks (white dots) with one standard deviation uncertainties on profile 2; vertical axis from 0 to 250 km depth. The locations of the profiles are shown in dark red in Figure 3a.

continuously across Alaska than in many prior studies. As seen in the profiles, the thickest crust in the maps lies beneath the Brooks Range (in the north of Figure 7) and where the Yakutat crust is most deeply underthrust (in the south). Variations in crustal thickness are associated with some major faults, for example, a northward decrease in crustal thickness across the eastern Denali fault (also resolved by Allam et al. (2017), Miller et al. (2018), Haney et al. (2020), and Mann et al. (2022)).

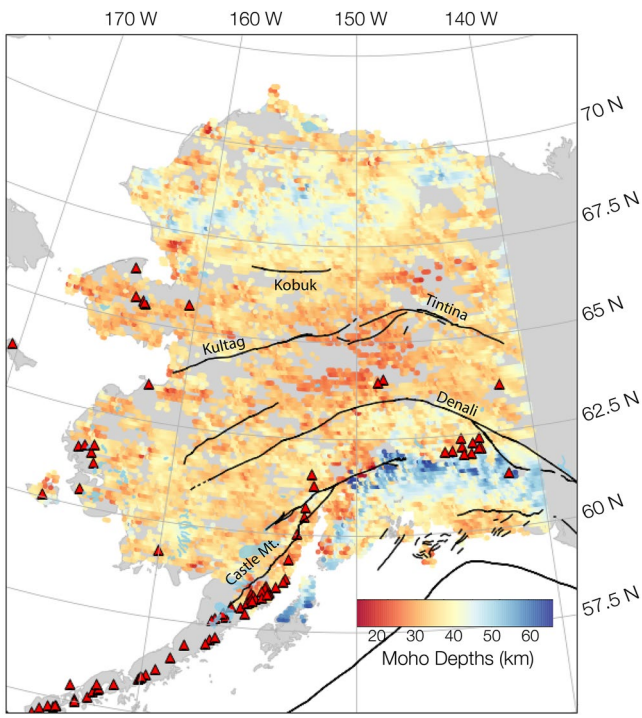

Figure 7. Map of Moho depths measured from the common conversion point stack. Volcanoes are indicated by red triangles and black lines are major faults (Elliott & Freymueller, 2020).

3.2. Lithosphere-Asthenosphere Boundary

At depths of 50–170 km, a negative phase in the CCP stack signifies a velocity decrease in the upper mantle. Based on our prior joint inversions of Sp and surface-wave phase velocities (Gama et al., 2021) and other tomography studies (e.g., Berg et al., 2020; Feng & Ritzwoller, 2019; Jiang et al., 2018; Martin-Short et al., 2018; Ward & Lin, 2018; Yang & Gao, 2020), we interpret this feature as the LAB.

The lithosphere is relatively thin in a broad swath of central Alaska (50–80 km) and the Seward Peninsula (~70 km), as seen in the map in Figure 8; the middle of the profiles in Figure 4, profiles A, B, and E; the western end of Figure 4, profile F; the northern side of Figure 5, profile C, and the western sides of Figure 5, profiles G and H. In contrast, the lithosphere is thicker in northernmost Alaska (120–170 km) beneath the northern Arctic-Alaska terrane (northern end of Figure 4, profiles A and B; middle of Figure 4, profile D). and also beneath the subducting plate in the east (~130 km) (eastern end of Figure 5, profile H). These broad patterns in relative lithospheric thickness are consistent with prior studies (e.g., Berg et al., 2020; Feng & Ritzwoller, 2019; Gama et al., 2021; Jiang et al., 2018; Martin-Short et al., 2018; O'Driscoll & Miller, 2015; Ward & Lin, 2018; Wang & Tape, 2014; Yang & Gao, 2020). In some regions of northern Alaska where the phase interpreted as the LAB is relatively deep, additional Sp energy consistent with negative velocity gradients lies at shallower mantle depths (e.g., the middle of profile D in Figure 5). These arrivals could signify

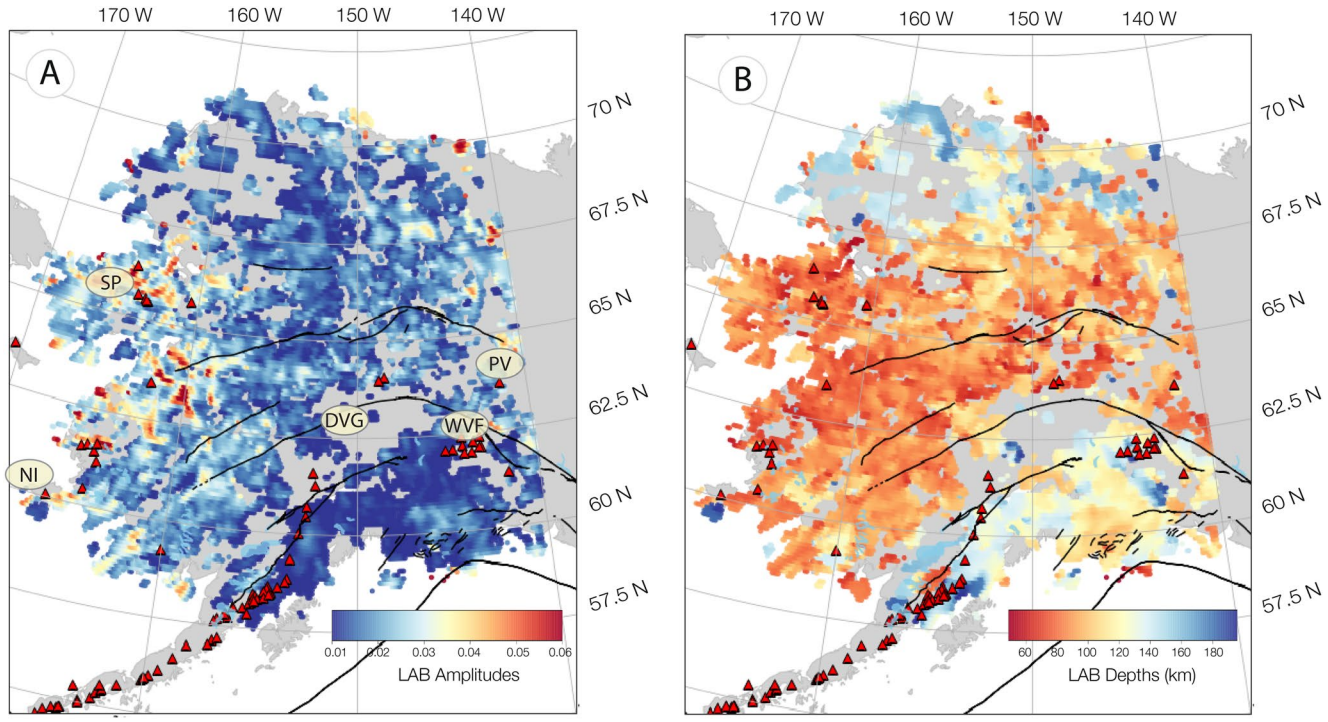

Figure 8. Maps of negative mantle velocity gradient (a) amplitudes and (b) depths measured from the common conversion point stack that we interpret as the lithosphere-asthenosphere boundary. Volcanoes are indicated by red triangles and black lines are major faults (Elliott & Freymueller, 2020). SP—Seward Peninsula; NI—Nunivak Island; WVF—Wrangell Volcanic Field; DVG—Denali Volcanic Gap; and PV—Prindle Volcano.

the presence of velocity layering within the mantle lithosphere, as has been observed in some cratonic mantles (e.g., Abt et al., 2010; S. M. Hansen et al., 2015; Krueger et al., 2021; Miller & Eaton, 2010).

In terms of amplitudes, Sp phases from the negative velocity gradient at the base of the upper plate are strongest in west-central Alaska, where LAB depths are shallower, as seen in Figure 8. Joint inversions of Sp data at single stations with Rayleigh phase velocities show comparable LAB depths and low asthenospheric velocities (Gama et al., 2021). Given that partial melt in the asthenosphere has been invoked to explain particularly strong LAB velocity gradients (e.g., Hopper et al., 2014; Rondenay et al., 2010; Rychert et al., 2013, 2018a, 2018b), we tested whether the LAB phase has a systematically larger amplitude near back-arc volcanoes (i.e., excluding volcanoes that lie above subducting plate seismicity). It does not. The mean amplitude of the LAB phase within a 50 km radius of all back-arc volcanoes and the mean amplitude of all points are not significantly different. Assuming that LAB amplitude is related to the presence of partial melt below the base of the plate, this result suggests either that partial melt does not collect in greater percentages beneath volcanic centers than elsewhere, or that the effects of partial melt beneath volcanic centers cancel out; in the latter case, more partial melt could collect below the LAB beneath some volcanic centers (creating a higher amplitude negative velocity gradient) but beneath other volcanic centers partial melt could intrude the lower lithosphere (reducing the negative velocity gradient at the LAB).

3.3. Mantle Positive Velocity Gradient

Below the lithosphere, we see a Sp phase corresponding to a positive mantle velocity gradient (the PVGm) (maps of depth and amplitude in Figure 9). This velocity gradient and the LAB above it are strongest and most coherent in western Alaska, including magmatically active regions such as the Seward Peninsula (e.g., left/west of Figure 4, profile E). However, higher amplitudes are also found in eastern Alaska at its central latitudes (e.g., right of Figure 4, profile E and Figure 5, profile C). Similar to the LAB calculation, magmatically active regions (within 20 km of volcanoes outside the main arc volcanic chain) do not show average phase amplitudes that are significantly different from the mean value of all PVGm picks. This result suggests that the process that produces the PVGm, possibly the onset of partial melting, is not spatially localized beneath volcanic centers. Based on

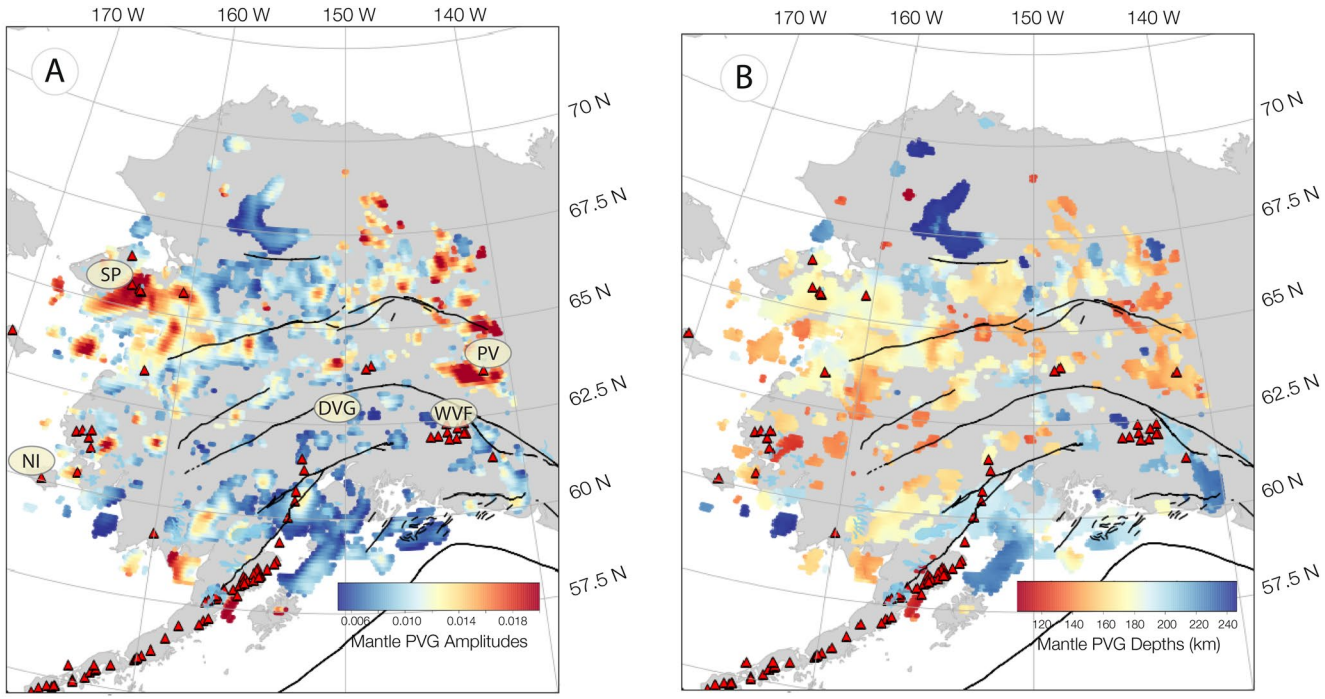

Figure 9. Maps of the deeper positive mantle velocity gradient (a) amplitudes and (b) depths measured from the common conversion point stack. Volcanoes are indicated by red triangles and black lines are major faults (Elliott & Freymueller, 2020). SP—Seward Peninsula; NI—Nunivak Island; WVF—Wrangell Volcanic Field; DVG—Denali Volcanic Gap; and PV—Prindle Volcano.

comparisons with shear wave velocity structure obtained by inverting surface wave data at periods that resolve structure in the PVGm depth range (e.g., Gama et al., 2021; Martin-Short et al., 2018), we interpreted this positive mantle phase as the lower boundary of a low-velocity asthenospheric layer.

4. Implications for Subduction, Mantle Flow, and Melting Beneath Alaska

The overall picture provided by the Moho and mantle discontinuities that appear in the Sp CCP stack (Figure 10) includes: the subduction of the Pacific lithosphere with a well-defined LAB; the thickest crust associated with the underthrust Yakutat terrane (seen more clearly in Figures 4 and 5); the thinnest lithosphere just north of subduction zone seismicity; the thickest lithosphere beneath northern Alaska, including thickened crust beneath the Brooks range; deeper PVGs marking the base of a low-velocity layer which lies within the asthenosphere.

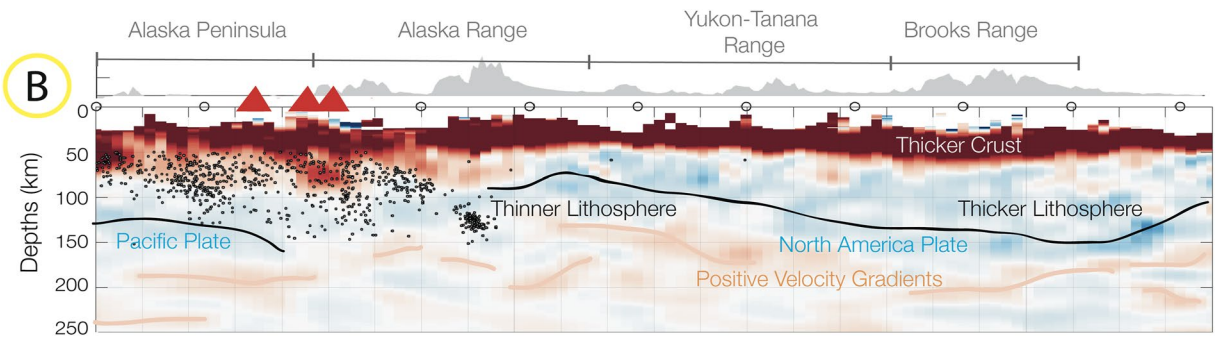

Figure 10. Interpretation of crust and mantle structure shown on a N-S profile (Figure 4, profile B) beneath Alaska. Black line highlights the negative velocity gradient interpreted as the lithosphere-asthenosphere boundary. Red lines highlight deeper positive velocity gradients, the strongest of which is the PVGm positive mantle velocity gradient.

4.1. Variations in Lithosphere Thickness

The thinnest lithosphere, observed in central Alaska, likely represents modification of the upper plate by subduction-derived processes, such as melting in the wedge associated with mantle wedge flow. This interpretation is consistent with the position of this zone just to the north of the deepest seismicity associated with the downgoing plate (Figure 4, profile F; Figure 5, profiles G and H) and low asthenospheric velocities (Gama et al., 2021). The LAB phase is typically absent, as expected, where the subducting lithosphere intersects the LAB depth range (Figure 8). Profile H (Figure 5) is an exception, likely reflecting the tendency of CCP stacking to horizontally smooth velocity discontinuities. An interesting nuance is that the LAB phase is also weak directly above the deepest seismicity (e.g., Figure 4, profile F; Figure 5, profile H; Figure 8). Some of this amplitude reduction may be due to interference between conversions from the top of the subducting lithosphere with the upper plate LAB. However, if the LAB amplitude reduction does reflect real structure, it suggests disruption of a pronounced negative velocity gradient at the base of the upper plate by rising melt and slab-derived fluids which lower upper plate velocities. However, such LAB disruption is less apparent within the Denali Volcanic Gap (Figure 5, profile G), perhaps due to cooler temperatures in the mantle wedge (Martin-Short et al., 2018; Rondenay et al., 2010), anomalously shallow release of volatiles (Chuang et al., 2017) or both (Yang & Gao, 2020) that result in lower amounts of partial melt production in the mantle wedge.

However, the thin upper plate lithosphere extends far northwest of the subducting plate to the Seward Peninsula, where low asthenospheric shear velocities (Gama et al., 2021) and surface magmatism also occur, requiring additional explanation (Figure 8b; Figure 4, profile E). The thin lithosphere is likely in part due to tectonic history. The Seward Peninsula and its immediate surroundings experienced significant extension at 130–70 Ma (Amato et al., 2003; Dumitru et al., 1995; Hannula et al., 1995). Nonetheless, the fact that the lithosphere remains thin today and the ongoing history of magmatism require more recent processes.

Relatively recent extension and mantle upwelling are one possible explanation for the thin lithosphere beneath the Seward Peninsula, In contrast to Quaternary magmas in the arc of the Alaskan subduction zone and the Wrangell Volcanic Field, which bear geochemical signatures of subduction (e.g., Andronikov & Mukasa, 2010; Nye et al., 2018; Preece & Hart, 2004; Richter et al., 1990; Trop et al., 2021), the young magmas of the Seward Peninsula and other sites in Alaska bordering the Bering Sea and extending to Nunivak Island (Figure 1) are consistent with a mantle source that overlaps ocean island basalts (Moll-Stalcup, 1994). However, these Bering Sea group magmas do not manifest a spatial age progression indicative of one or more hotspots; rather, they have been attributed to decompression in upwelling flow related to lithospheric extension (Mukasa et al., 2007). Estimates of active deformation are consistent with extension, given that the Seward Peninsula is pulling away to the southwest from northern Alaska; this extension is part of a regional pattern of surface velocities that includes the westward extrusion of southwestern Alaska (Elliott & Freymueller, 2020). Geodynamical modeling (e.g., Finzel et al., 2015; Jadamec & Billen, 2012; Jadamec et al., 2013, 2018) as well as mantle azimuthal anisotropy (e.g., McPherson et al., 2020; Venereau et al., 2019) indicate strongly three-dimensional mantle flow associated with this surface deformation. Ongoing extension, potential upwelling within three-dimensional asthenospheric flow and the partial melt it generates provide potential mechanisms for maintaining the thin lithosphere beneath the Seward Peninsula.

The relatively thin lithosphere found in interior Alaska, extending north to the southern edge of the Brooks Range and the northern Arctic-Alaska terrane (Figure 4, profile A; Figure 8b), also requires an explanation. Lithospheric extension has likely played a role. Interior Alaska south of the Brooks Range experienced significant extension and magmatism not only during the mid-Cretaceous (130–90 Ma) (Miller & Hudson, 1991), but also during the Eocene (Andronikov & Mukasa, 2010; Dusel-Bacon & Murphy, 2001), and the later rifting may be related to decompression melting as seen in the Fort Hamlin Hills basalts that erupted south of the Brooks Range at ∼31 Ma (Andronikov & Mukasa, 2010). However, while minor extension appears to be present in this region in the present-day (Elliott & Freymueller, 2020) its rates are small, and this region does not contain the active magmatism seen in the Seward Peninsula. Alternatively, lithospheric foundering processes, such as delamination or viscous downwelling at the edge of the thick lithosphere beneath the northern Arctic Alaska terrane (e.g., King & Ritsema, 2000; Van Wijk et al., 2008), may have contributed to thinning the upper plate lithosphere. Consequences of foundering include decompression melting from the asthenosphere that rises in response to downwelling and zones of crustal extension (e.g., Göğüş & Pysklywec, 2008), possibly explaining these phenomena south of the Brooks Range during and just after the Eocene (Andronikov & Mukasa, 2010;

Dusel-Bacon & Murphy, 2001). Lithospheric thinning due to foundering is also a possibility beneath the Seward Peninsula. If lithospheric foundering did occur in interior Alaska, or beneath the Seward Peninsula, continued vigorous three-dimensional mantle flow (e.g., Finzel et al., 2015; Jadamec et al., 2013) has likely helped maintain a relatively thin lithosphere at these latitudes since the initial lithospheric thinning occurred.

In contrast, the thick lithosphere indicated by the deep LAB phases beneath the Brooks Range and the northern Arctic-Alaska terrane is cold, as shown by its high absolute velocities (e.g., Gama et al., 2021), which are similar to the global average for Archean cratons (French et al., 2013) where xenoliths document cool geotherms (e.g., Lee et al., 2011). Cool geotherms are corroborated by the low heat flow beneath all but the northern tip of the northern Arctic-Alaska terrane (Batir et al., 2016). In addition, this region of thick lithosphere is characterized by low surface deformation rates based on geodetic and fault slip data (e.g., Elliott & Freymueller, 2020; Finzel et al., 2015) and has been characterized as having high mantle viscosity (Finzel et al., 2015). Seismicity rates are low beneath most of the northern Arctic Alaska terrane (e.g., Ruppert & West, 2019), consistent with minimal deformation. A 2018 earthquake swarm north of the Brooks Range is an exception (Ruppert & West, 2019), but these events are located in a zone where the picked LAB phase partly lies at shallower depths, perhaps indicating an anomaly within the otherwise thicker lithosphere. Beneath much of the thick lithosphere in the north, the LAB phase is too weak to meet the criteria for depth measurements as described in Section 3 (e.g., Hua, Fischer, Wu, & Blom, 2020). This is likely because the LAB velocity gradient is more gradual, for example, occurring over depths of 50 km or more (Gama et al., 2021), which makes it harder to identify the LAB with converted waves (e.g., Ford et al., 2010; Rychert et al., 2007). The deep LAB observed beneath the subducting plate in the east (~120 km) (also seen in O'Driscoll and Miller (2015) and Gama et al. (2021)) can be modeled as an oceanic plate that has cooled typically (Hasterok, 2013) for its age, plus the additional thickness of the crust of the Yakutat terrane (e.g., Christeson et al., 2013; Fuis et al., 2008; Gama et al., 2021; Müller et al., 2008).

4.2. Patterns of Positive Velocity Gradients

Mantle PVGs in a similar depth range to those we observe beneath Alaska have been imaged in other regions, primarily zones characterized by high mantle temperatures and magmatic activity, including Hawaii (Rychert et al., 2013), the Canary hotspot (Miller et al., 2015), the young Juan de Fuca plate (Rychert et al., 2018a, 2018b), the northwestern U.S. (Hopper et al., 2014), Anatolia (Hua, Fischer, Wu, & Blom, 2020), and the eastern Iranian plateau (Wu et al., 2021), and high high-temperature mantle globally (Hua et al., 2021), leading to their interpretation as the lower boundaries of low-velocity layers of asthenosphere that contains partial melt. In Alaska, two aspects of the PVGm distribution support its interpretation as the base of a melt-bearing mantle layer. First, the PVGm drops in amplitude and fades away beneath the thicker lithosphere in northern Alaska, which appears to be a lower temperature region based on its high seismic velocities (e.g., Gama et al., 2021; Martin-Short et al., 2018) and low heat flow (Batir et al., 2016). Second, the spatial correlation of higher amplitude Sp energy from the PVGm with higher LAB amplitudes (e.g., the Bering Sea margin from Nunivak Island to the Seward Peninsula and east-central Alaska; Figures 8a and 9a) are consistent with the idea the clear PVGm arrivals are due to the presence of partial melt, since melt could sharpen velocity gradients at both the top and bottom of a melt-bearing layer. The observation that LAB and PVGm amplitudes do not, on average, increase locally beneath volcanoes (Sections 3.2 and 3.3) suggests that partial melt is widely distributed within the apparent low-velocity layer, with the caveat that there could be competing effects of melt on LAB amplitudes (enhancement by pooling of partial melt below the upper plate and reduction by melt infiltration into the base of the plate (Section 3.2)).

Above and adjacent to subducting lithosphere in the Alaskan subduction zone and the Wrangell Volcanic Field, Quaternary magma compositions (e.g., Andronikov & Mukasa, 2010; Nye et al., 2018; Preece & Hart, 2004; Richter et al., 1990; Trop et al., 2021) are consistent with the presence of partial melt as a result of subduction zone processes. These processes include slab dehydration, melting in the mantle wedge, and mantle wedge flow (e.g., Grove et al., 2009; Wang et al., 2020). For example, the model of Wang et al. (2020) indicates a partial melt bearing zone within the mantle wedge whose lower boundary (the wet solidus) would be comparable in depth to the Alaskan mantle PVGm, and whose upper boundary (also the wet solidus) corresponds to observed LAB depths. Alternatively, the PVGm could represent a melting front related to carbon-assisted melting (Chen et al., 2016; Dasgupta & Hirschmann, 2010; Duke et al., 2014; Hammouda & Laporte, 2000; Hammouda et al., 2021; Sifré et al., 2014). In particular, Hammouda et al. (2021) invoke a redox boundary at depths comparable to the Alaskan PVGm that would allow partial melt to be stable between this boundary and the LAB.

Above the northwest-dipping seismicity in the Alaskan subduction zone, the PVGm has a higher amplitude close to the subducting plate in the southwest and is low amplitude, sporadic, or absent in the northeast, including in the Denali Volcanic Gap (Figure 9a). This variation may relate to the decrease in slab dip to the northeast. For example, Grove et al. (2009) point out that as slab dip decreases, the lateral extent of the melting region widens, potentially reducing partial melt fractions and decreasing the amplitude of the PVGm associated with the base of the melting layer. In addition, as previously mentioned, the Denali Volcanic Gap mantle wedge may be colder or be the site of anomalously shallow release of volatiles (Chuang et al., 2017; Martin-Short et al., 2018; Rondenay et al., 2010; Yang & Gao, 2020).

In the vicinity of the Wrangell Volcanic Field, seismicity (Daly et al., 2021), imaging of the downgoing plate through migration of Ps phases (Mann et al., 2022), and attenuation measurements all argue for northeast-directed subduction. These results, in combination with signatures of subduction in Quaternary magmas (e.g., Andronikov & Mukasa, 2010; Nye et al., 2018; Preece & Hart, 2004; Richter et al., 1990; Trop et al., 2021), indicate that the PVGm in this region can also be explained as the base of a subduction-related melting zone.

In the zones of highest PVGm amplitudes, which lie farther from the subducting lithosphere, Quaternary magmas do not manifest signatures typical of subduction zone arcs; instead, they are consistent with basaltic decompression melting (Andronikov & Mukasa, 2010; Mukasa et al., 2007; Nye et al., 2018). As previously described (Section 4.1), between Nunivak Island and the Seward Peninsula, where one of the high amplitude PVGm (and LAB velocity gradient) zones lies (Figure 9a), Quaternary magmas are consistent with an ocean island basalt source and decompression melting in upwelling mantle flow (Moll-Stalcup, 1994; Mukasa et al., 2007), and the upwelling flow could be created by lithospheric extension related to the extrusion of southwestern Alaska (Elliott & Freymueller, 2020). In the second region of high PVGm amplitude, which lies in eastern Alaska north of ~63°N, Prindle volcano is the only Quaternary volcanic center (Figure 9a), and while its composition differs from the Alaskan arc and is more consistent with decompression melting, it still bears some signatures of subduction (Andronikov & Mukasa, 2010; Nye et al., 2018). The decompression here could be created by an upwelling component to asthenospheric flow that is circulating counter-clockwise around the edge of the subducting lithosphere (e.g., Jadamec & Billen, 2012; Jadamec et al., 2013, 2018), possibly in combination with flow through a slab tear (e.g., Fuis et al., 2008; Gou et al., 2019; Jiang et al., 2018). A melting front at ~150 km depth that produces an observable PVGm can be created with only modest water content (<200 wt ppm) and mantle potential temperatures that overlap the range for ambient mantle as represented by mid-ocean ridges (Bao et al., 2022; Hua et al., 2021). In addition, if carbon-assisted melting is considered, the redox front proposed by Hammouda et al. (2021) could explain the depths of the PVGm observed in these regions (Figure 9b).

Elsewhere, weak and sporadic PVGm phases are observed beneath the subducting lithosphere and beneath a small portion of the thick lithosphere in northern Alaska, sometimes at depths greater than 200 km (Figure 9). If mantle melting plays a role in producing these velocity gradients, the base of a layer containing carbon-assisted partial melt is a candidate explanation (e.g., Hammouda et al., 2021), if oxidized mantle extends to the depth of the PVGm.

5. Conclusions

Common conversion point stacking of Sp phases recorded in Alaska by NSF EarthScope TA stations and other networks has provided new insight on crust and mantle discontinuities associated with the North American and subducting plates.

Nearly continuous measurements of Moho depth delineate the margin of the thick crust of the underthrust Yakutat terrane, a marked decrease in crustal thickness to the north across the Denali fault, and the thickened crustal root beneath the Brooks Range in the north.

New constraints on the negative velocity gradient at the LAB outline a zone of particularly thin lithosphere in the back-arc direction just beyond the position of the deepest seismicity in the Alaskan subduction zone, consistent with thinning of the upper plate by subduction zone flow and melt rising from the mantle wedge. Directly above the deepest seismicity, LAB amplitude drops, likely due to greater infiltration of melt and heat into the upper plate that decreases the velocity contrast between lithosphere and asthenosphere.

Thin lithosphere continues far northwest and north of the subduction zone, including the Seward Peninsula and reaching the southern edge of the Brooks Range, where it meets thicker, colder, and higher viscosity lithosphere beneath the northern Arctic Alaska terrane. While past extensional tectonics—and possibly lithospheric foundering—could have contributed to thinning the lithosphere beneath the Seward Peninsula and interior Alaska, ongoing ablation of the upper plate by asthenospheric flow likely helps to keep the lithosphere thin.

A particularly novel structure imaged in this study is a PVG that represents the base of a low velocity layer of asthenospheric mantle whose upper boundary corresponds to the LAB. Closer to the subducting lithosphere, this gradient could represent the onset of partial melting enabled by slab-derived fluids, with or without an assist from carbon in the mantle. However, this PVG is strongest further away from the subduction zone, beneath the Seward Peninsula and to the northeast of the Wrangell Volcanic Field, suggesting the presence of partial melt in the asthenosphere hundreds of kilometers away from the slab. Magmas in these locations indicate decompression melting, consistent with components of upwelling asthenosphere.

Data Availability Statement

Waveform data employed in this study were obtained from the Incorporated Research Institutions for Seismology (IRIS) Data Management System. This work employed data from the NSF EarthScope Transportable Array (TA, https://doi.org/10.7914/SN/TA), the Alaska Regional Seismic Network (AK, https://doi.org/10.7914/SN/AK), the IRIS/USGS and IRIS/IDA stations of the Global Seismographic Network (IU, https://doi.org/10.7914/SN/IU and II, https://doi.org/10.7914/SN/II), the USGS Advanced National Seismic System (US https://doi.org/10.7914/SN/US), the National Tsunami Warning Center Alaska Seismic Network (AT, https://doi.org/10.7914/SN/AT), the Alaska Volcano Observatory (AV, https://doi.org/10.7914/SN/AV), the Digital World-Wide Standardized Seismograph Network (DW, https://doi.org/10.7914/SN/DW), and International Miscellaneous Stations (IM). Waveforms were also included from the Broadband Experiment Across the Alaska Range (BEAAR) (XE, https://doi.org/10.7914/SN/XE_1999), the ARCTIC array (XR, https://doi.org/10.7914/SN/XR_2004), the St. Elias Erosion/Tectonics Project (STEEP) (XZ, https://doi.org/10.7914/SN/XZ_2005), the Denali Fault Aftershocks RAMP (YM, https://doi.org/10.7914/SN/YM_2002), Multidisciplinary Observations of Subduction (MOOS) (YV, https://doi.org/10.7914/SN/YV_2006), A Four-dimensional View of Deformation in the Eastern Alaska Range (Z5, https://doi.org/10.7914/SN/Z5_2018), and the PN, PP, YE, and YG network codes. Files containing Moho, LAB, and PVGm depths and uncertainties are available on the Brown University Digital Data Repository (https://doi.org/10.26300/zgwd-x886).

Acknowledgments
We thank Alberto Saal and Joe McConeghy for great discussions, Michael Mann and Geoffrey A. Abers for volcano and seismicity data, and Julie Elliott for fault data. This research was supported by the NSF EarthScope Program (EAR-1829401).

References

Abers, G. A., Fischer, K. M., Hirth, G., Wiens, D. A., Plank, T., Holtzman, B. K., et al. (2014). Reconciling mantle attenuation-temperature relationships from seismology, petrology, and laboratory measurements. *Geochemistry, Geophysics, Geosystems*, *15*(9), 3521–3542. https://doi.org/10.1002/2014GC005444

Abt, D. L., Fischer, K. M., French, S. W., Ford, H. A., Yuan, H., & Romanowicz, B. (2010). North American lithospheric discontinuity structure imaged by Ps and Sp receiver functions. *Journal of Geophysical Research*, *115*(B9), B09301. https://doi.org/10.1029/2009JB006914

Allam, A. A., Schulte-Pelkum, V., Ben-Zion, Y., Tape, C., Ruppert, N., & Ross, Z. E. (2017). Ten kilometer vertical Moho offset and shallow velocity contrast along the Denali fault zone from double-difference tomography, receiver functions, and fault zone head waves. *Tectonophysics*, *721*, 56–69. https://doi.org/10.1016/j.tecto.2017.09.003

Amante, C., & Eakins, B. W. (2009). *ETOPO1 1 arc-minute global relief model: Procedures, data sources and analysis*. NOAA Technical Memorandum NESDIS NGDC-24. National Geophysical Data Center, NOAA. https://doi.org/10.7289/V5C8276M

Amato, J. M., Miller, E. L., Wright, J. E., & McIntosh, W. C. (2003). Dike swarms on Seward Peninsula, Alaska, and their implications for the kinematics of Cretaceous extension in the Bering Strait region. *Canadian Journal of Earth Sciences*, *40*(6), 865–886. https://doi.org/10.1139/e03-019

Andronikov, A. V., & Mukasa, S. B. (2010). $^{40}Ar/^{39}Ar$ eruption ages and geochemical characteristics of Late Tertiary to Quaternary intraplate and arc-related lavas in interior Alaska. *Lithos*, *115*(1–4), 1–14. https://doi.org/10.1016/j.lithos.2009.11.002

Bao, X., Lithgow-Bertelloni, C. R., Jackson, M. G., & Romanowicz, B. (2022). On the relative temperatures of Earth's volcanic hotspots and mid-ocean ridges. *Science*, *375*(6576), 57–61. https://doi.org/10.1126/science.abj8944

Batir, J. F., Blackwell, D. D., & Richards, M. C. (2016). Heat flow and temperature-depth curves throughout Alaska: Finding regions for future geothermal exploration. *Journal of Geophysics and Engineering*, *13*(3), 366–378. https://doi.org/10.1088/1742-2132/13/3/366

Bauer, M. A., Pavlis, G. L., & Landes, M. (2014). Subduction geometry of the Yakutat terrane, southeastern Alaska. *Geosphere*, *10*(6), 1161–1176. https://doi.org/10.1130/GES00852

Berg, E. M., Lin, F.-C., Allam, A., Schulte-Pelkum, V., Ward, K. M., & Shen, W. (2020). Shear velocity model of Alaska via joint inversion of Rayleigh wave ellipticity, phase velocities, and receiver functions across the Alaska Transportable Array. *Journal of Geophysical Research: Solid Earth*, *125*(2), e2019JB018582. https://doi.org/10.1029/2019JB018582

Bodin, T., Yuan, H., & Romanowicz, B. (2013). Inversion of receiver functions without deconvolution—Application to the Indian craton. *Geophysical Journal International*, *196*(2), ggt431–1033. https://doi.org/10.1093/gji/ggt431

Brennan, P. R., Gilbert, H., & Ridgway, K. D. (2011). Crustal structure across the central Alaska Range: Anatomy of a Mesozoic collisional zone. *Geochemistry, Geophysics, Geosystems*, *12*(4), 1–23. https://doi.org/10.1029/2011GC003519

Calo, M., Bodin, T., & Romanowicz, B. (2016). Layered structure in the upper mantle across North America from joint inversion of long and short period seismic data. *Earth and Planetary Science Letters*, *449*, 164–175. https://doi.org/10.1016/j.epsl.2016.05.054

Chen, C. F., Liu, Y. S., Foley, S. F., Ducea, M. N., He, D. T., Hu, Z. C., et al. (2016). Paleo-Asian oceanic slab under the North China craton revealed by carbonatites derived from subducted limestones. *Geology*, *44*(12), 1039–1042. https://doi.org/10.1130/g38365.1

Chesley, C., Key, K., Constable, S., Behrens, J., & MacGregor, L. (2019). Crustal cracks and frozen flow in oceanic lithosphere inferred from electrical anisotropy. *Geochemistry, Geophysics, Geosystems*, *20*(12), 5979–5999. https://doi.org/10.1029/2019GC008628

Christeson, G. L., Van Avendonk, H. J. A., Gulick, S. P. S., Reece, R. S., Pavlis, G. L., & Pavlis, T. L. (2013). Moho interface beneath Yakutat terrane, southern Alaska. *Journal of Geophysical Research: Solid Earth*, *118*(9), 5084–5097. https://doi.org/10.1002/jgrb.50361

Chuang, L., Bostock, M., Wech, A., & Plourde, A. (2017). Plateau subduction, intraslab seismicity, and the Denali (Alaska) volcanic gap. *Geology*, *45*(7), 647–650. https://doi.org/10.1130/g38867.1

Daly, K., Abers, G. A., Mann, M. E., Roecker, S. R., & Christensen, D. H. (2021). Subduction of an oceanic plateau across southcentral Alaska: High-resolution seismicity. *Journal of Geophysical Research: Solid Earth*, *126*(11), e2021JB022809. https://doi.org/10.1029/2021JB022809

Dasgupta, R. (2018). Volatile-bearing partial melts beneath oceans and continents-where, how much, and of what compositions? *American Journal of Science*, *318*(1), 141–165. https://doi.org/10.2475/01.2018.06

Dasgupta, R., & Hirschmann, M. M. (2010). The deep carbon cycle and melting in Earth's interior. *Earth and Planetary Science Letters*, *298*(1–2), 1–13. https://doi.org/10.1016/j.epsl.2010.06.039

Dueker, K. G., & Sheehan, A. F. (1997). Mantle discontinuity structure from midpoint stacks of converted P to S waves across the Yellowstone hotspot track. *Journal of Geophysical Research*, *102*(B4), 8313–8327. https://doi.org/10.1029/96jb03857

Duke, G. I., Carlson, R. W., Frost, C. D., Hearn, B. C., Jr., & Eby, G. N. (2014). Continent-scale linearity of kimberlite-carbonatite magmatism, mid-continent North America. *Earth and Planetary Science Letters*, *403*, 1–14. https://doi.org/10.1016/j.epsl.2014.06.023

Dumitru, T. A., Miller, E. L., O'Sullivan, P. B., Amato, J. M., Hannula, K. A., Calvert, A. T., & Gans, P. B. (1995). Cretaceous to Recent extension in the Bering Strait region, Alaska. *Tectonics*, *14*(3), 549–563. https://doi.org/10.1029/95tc00206

Dusel-Bacon, C., & Murphy, J. M. (2001). Apatite fission track evidence of widespread Eocene heating and exhumation in the Yukon-Tanana Upland, interior Alaska. *Canadian Journal of Earth Sciences*, *38*(8), 1191–1204. https://doi.org/10.1139/e01-015

Eberhart-Phillips, D., Christensen, D. H., Brocher, T. M., Hansen, R., Ruppert, N. A., Haeussler, P. J., & Abers, G. A. (2006). Imaging the transition from Aleutian subduction to Yakutat collision in central Alaska, with local earthquakes and active source data. *Journal of Geophysical Research*, *111*(11), 1–31. https://doi.org/10.1029/2005JB004240

Eilon, Z., Fischer, K. M., & Dalton, C. A. (2018). An adaptive Bayesian inversion for upper-mantle structure using surface waves and scattered body waves. *Geophysical Journal International*, *214*(1), 232–253. https://doi.org/10.1093/gji/ggy137

Elliott, J., & Freymueller, J. T. (2020). A block model of present-day kinematics of Alaska and western Canada. *Journal of Geophysical Research: Solid Earth*, *125*(7), e2019JB018378. https://doi.org/10.1029/2019JB018378

Feng, L. (2021). Amphibious shear wave structure beneath the Alaska-Aleutian subduction zone from ambient noise tomography. *Geochemistry, Geophysics, Geosystems*, *22*(5), e2020GC009438. https://doi.org/10.1029/2020gc009438

Feng, L., & Ritzwoller, M. H. (2019). A 3-D shear velocity model of the crust and uppermost mantle beneath Alaska including apparent radial anisotropy. *Journal of Geophysical Research: Solid Earth*, *124*(10), 10468–10497. https://doi.org/10.1029/2019jb018122

Ferris, A., Abers, G. A., Christensen, D. H., & Veenstra, E. (2003). High resolution image of the subducted Pacific plate beneath central Alaska, 50–150 km depth. *Earth and Planetary Science Letters*, *214*(3–4), 575–588. https://doi.org/10.1016/s0012-821x(03)00403-5

Finzel, E. S., Flesch, L. M., Ridgway, K. D., Holt, W. E., & Ghosh, A. (2015). Surface motions and intraplate continental deformation in Alaska driven by mantle flow. *Geophysical Research Letters*, *42*(11), 4350–4358. https://doi.org/10.1002/2015GL063987

Fischer, K. M., Rychert, C. A., Dalton, C. A., Miller, M. S., Beghein, C., & Schutt, D. L. (2020). A comparison of oceanic and continental mantle lithosphere. *Physics of the Earth and Planetary Interiors*, *309*, 106600. https://doi.org/10.1016/j.pepi.2020.106600

Ford, H. A., Fischer, K. M., Abt, D. L., Rychert, C. A., & Elkins-Tanton, L. T. (2010). The lithosphere-asthenosphere boundary and cratonic lithospheric layering beneath Australia from Sp wave imaging. *Earth and Planetary Science Letters*, *300*(3–4), 299–310. https://doi.org/10.1016/j.epsl.2010.10.007

French, S., Lekić, V., & Romanowicz, B. (2013). Waveform tomography reveals channeled flow at the base of the oceanic asthenosphere. *Science*, *342*(6155), 227–230. https://doi.org/10.1126/science.1241514

Fuis, G. S., Moore, T. E., Plafker, G., Brocher, T. M., Fisher, M. A., Mooney, W. D., et al. (2008). Trans-Alaska crustal transect and continental evolution involving subduction underplating and synchronous foreland thrusting. *Geology*, *36*(3), 267–270. https://doi.org/10.1130/G24257A.1

Gama, I., Fischer, K. M., Eilon, Z., Krueger, H. E., Dalton, C. A., & Flesch, L. M. (2021). Shear-wave velocity structure beneath Alaska from a Bayesian joint inversion of Sp receiver functions and Rayleigh wave phase velocities. *Earth and Planetary Science Letters*, *560*, 116785. https://doi.org/10.1016/j.epsl.2021.116785

Göğüş, O. H., & Pysklywec, R. N. (2008). Near-surface diagnostics of dripping or delaminating lithosphere. *Journal of Geophysical Research*, *113*(B11), B11404. https://doi.org/10.1029/2007JB005123

Golos, E. M., & Fischer, K. M. (2022). New insights into lithospheric structure and melting beneath the Colorado Plateau. *Geochemistry, Geophysics, Geosystems*, *23*(3), e2021GC010252. https://doi.org/10.1029/2021GC010252

Gou, T., Zhao, D., Huang, Z., & Wang, L. (2019). Aseismic deep slab and mantle flow beneath Alaska: Insight from anisotropic tomography. *Journal of Geophysical Research: Solid Earth*, *124*(2), 1700–1724. https://doi.org/10.1029/2018JB016639

Grove, T. L., Till, C. B., Lev, E., Chatterjee, N., & Medard, E. (2009). Kinematic variables and water transport control the formation and location of arc volcanoes. *Nature*, *459*(7247), 694–697. https://doi.org/10.1038/nature08044

Hammouda, T., & Laporte, D. (2000). Ultrafast mantle impregnation by carbonatite melts. *Geology*, *28*(3), 283–285. https://doi.org/10.1130/0091-7613(2000)28<283:umibcm>2.0.co;2

Hammouda, T., Manthilake, G., Goncalves, P., Chantel, J., Guignard, J., Crichton, W., & Gaillard, F. (2021). Is there a global carbonate layer in the oceanic mantle? *Geophysical Research Letters*, *48*(2), e2020GL089752. https://doi.org/10.1029/2020GL089752

Haney, M. M., Ward, K. M., Tsai, V. C., & Schmandt, B. (2020). Bulk structure of the crust and upper mantle beneath Alaska from an approximate Rayleigh-wave dispersion formula. *Seismological Society of America*, *91*(6), 3064–3075. https://doi.org/10.1785/0220200162

Hannula, K. A., Miller, E. L., Dumitru, T. A., Lee, J., & Rubin, C. M. (1995). Structural and metamorphic relations in the southwest Seward Peninsula, Alaska: Crustal extension and the unroofing of blueschists. *GSA Bulletin*, *107*(5), 536–553. https://doi.org/10.1130/0016-7606

Hansen, L. N., Qi, C., & Warren, J. M. (2016). Olivine anisotropy suggests Gutenberg discontinuity is not the base of the lithosphere. *Proceedings of the National Academy of Sciences of the United States of America*, *113*(38), 10503–10506. https://doi.org/10.1073/pnas.1608269113

Hansen, S. M., Dueker, K., & Schmandt, B. (2015). Thermal classification of lithospheric discontinuities beneath USArray. *Earth and Planetary Science Letters*, *431*, 36–47. https://doi.org/10.1016/j.epsl.2015.09.009
Hansen, S. M., & Schmandt, B. (2017). P and S wave receiver function imaging of subduction with scattering kernels. *Geochemistry, Geophysics, Geosystems*, *18*(12), 4487–4502. https://doi.org/10.1002/2017GC007120
Hasterok, D. (2013). A heat flow based cooling model for tectonic plates. *Earth and Planetary Science Letters*, *361*, 34–43. https://doi.org/10.1016/j.epsl.2012.10.036
Hayes, G. P., Moore, G. L., Portner, D. E., Hearne, M., Flamme, H., Furtney, M., & Smoczyk, G. M. (2018). Slab2, a comprehensive subduction zone geometry model. *Science*, *362*(6410), 58–61. https://doi.org/10.1126/science.aat4723
Hirschmann, M. M. (2010). Partial melt in the oceanic low velocity zone. *Physics of the Earth and Planetary Interiors*, *179*(1–2), 60–71. https://doi.org/10.1016/j.pepi.2009.12.003
Hirth, G., & Kohlstedt, D. (2003). Rheology of the upper mantle and the mantle wedge: A view from the experimentalists. In J. Eiler (Ed.), *Inside the subduction factory* (Vol. 138, pp. 83–105). Geophysical Monograph, American Geophysical Union.
Hopper, E., Ford, H. A., Fischer, K. M., Lekic, V., & Fouch, M. J. (2014). The lithosphere-asthenosphere boundary and the tectonic and magmatic history of the northwestern United States. *Earth and Planetary Science Letters*, *402*, 69–81. https://doi.org/10.1016/j.epsl.2013.12.016
Hua, J., Fischer, K. M., Mancinelli, N. J., & Bao, T. (2020). Imaging with pre-stack migration based on Sp scattering kernels. *Geophysical Journal International*, *220*(1), 428–449. https://doi.org/10.1093/gji/ggz459
Hua, J., Fischer, K. M., & Savage, M. K. (2018). The lithosphere-asthenosphere boundary beneath the South Island of New Zealand. *Earth and Planetary Science Letters*, *484*, 92–102. https://doi.org/10.1016/j.epsl.2017.12.011
Hua, J., Fischer, K. M., Wu, M., & Blom, N. A. (2020). New approaches to multifrequency Sp stacking tested in the Anatolian region. *Journal of Geophysical Research: Solid Earth*, *125*(11), e2020JB020313. https://doi.org/10.1029/2020JB020313
Hua, K., Fischer, K. M., Becker, T., Hirth, G., & Gazel, E. (2021). *Seismic detection and dynamical implications of ubiquitous asthenospheric partial melt*. Abstract DI14B-04 presented at 2021 Fall AGU Meeting, 13–17 Dec.
Jadamec, M. A., & Billen, M. I. (2012). The role of rheology and slab shape on rapid mantle flow: Three-dimensional numerical models of the Alaska slab edge. *Journal of Geophysical Research*, *117*(B2), B02304. https://doi.org/10.1029/2011jb008563
Jadamec, M. A., Billen, M. I., & Roeske, S. M. (2013). Three-dimensional numerical models of flat slab subduction and the Denali fault driving deformation in south-central Alaska. *Earth and Planetary Science Letters*, *376*, 29–42. https://doi.org/10.1016/j.epsl.2013.06.009
Jadamec, M. A., Kreylos, O., Chang, B., Fischer, K. M., & Yikilmaz, M. B. (2018). A visual survey of global slab geometries with show Earth model and implications for a three-dimensional subduction paradigm. *Earth and Space Science*, *5*(6), 240–257. https://doi.org/10.1002/2017ea000349
Jiang, C., Schmandt, B., Ward, K. M., Lin, F. C., & Worthington, L. L. (2018). Upper mantle seismic structure of Alaska from Rayleigh and S wave tomography. *Geophysical Research Letters*, *45*(19), 10350–10359. https://doi.org/10.1029/2018GL079406
Julia, J., Ammon, C. J., Herrmann, R. B., & Correig, A. M. (2000). Joint inversion of receiver function and surface wave dispersion observations. *Geophysical Journal*, *143*(1), 99–112. https://doi.org/10.1046/j.1365-246x.2000.00217.x
Karato, S.-I., & Park, J. (2018). On the origin of the upper mantle seismic discontinuities. In H. Yuan & B. A. Romanowicz (Eds.), *Lithospheric discontinuities* (Vol. 239. pp. 5–34). AGU Geophysical Monograph. https://doi.org/10.1002/9781119249740.ch8
Keith, C. M., & Crampin, S. (1977). Seismic body waves in anisotropic media: Synthetic seismograms. *Geophysical Journal of the Royal Astronomical Society*, *49*(1), 225–243. https://doi.org/10.1111/j.1365-246X.1977.tb03710.x
Kennett, B. L. N. (1991). The removal of free surface interactions from three-component seismograms. *Geophysical Journal International*, *104*(1), 153–163. https://doi.org/10.1111/j.1365-246x.1991.tb02501.x
Kim, Y., Abers, G. A., Li, J., Christensen, D., Calkins, J., & Rondenay, S. (2014). Alaska Megathrust 2: Imaging the megathrust zone and Yakutat/Pacific plate interface in the Alaska subduction zone. *Journal of Geophysical Research: Solid Earth*, *119*(3), 1924–1941. https://doi.org/10.1002/2013jb010581
Kind, R., Sodoudi, F., Yuan, X., Shomali, H., Roberts, R., Gee, D., et al. (2013). Scandinavia: A former Tibet? *Geochemistry, Geophysics, Geosystems*, *14*(10), 4479–4487. https://doi.org/10.1002/ggge.20251
King, S. D., & Ritsema, J. (2000). African hot spot volcanism: Small-scale convection in the upper mantle beneath cratons. *Science*, *290*(5494), 1137–1140. https://doi.org/10.1126/science.290.5494.1137
Krueger, H. E., Gama, I., & Fischer, K. M. (2021). Global patterns in cratonic mid-lithospheric discontinuities from Sp receiver functions. *Geochemistry, Geophysics, Geosystems*, *22*(6), e2021GC009819. https://doi.org/10.1029/2021gc009819
Lee, C. T. A., Luffi, P., & Chin, E. J. (2011). Building and destroying continental mantle. *Annual Review of Earth and Planetary Sciences*, *39*(1), 59–90. https://doi.org/10.1146/annurev-earth-040610-133505
Lekić, V., & Fischer, K. M. (2014). Contrasting lithospheric signatures across the western United States revealed by Sp receiver functions. *Earth and Planetary Science Letters*, *402*, 90–98. https://doi.org/10.1016/j.epsl.2013.11.026
Lekić, V., & Fischer, K. M. (2017). Interpreting spatially stacked Sp receiver functions. *Geophysical Journal International*, *210*(2), 874–886. https://doi.org/10.1093/gji/ggx206
Ligorría, J., & Ammon, C. (1999). Iterative deconvolution and receiver function estimation. *Bulletin of the Seismological Society of America*, *89*(5), 1395–1400. https://doi.org/10.1785/bssa0890051395
Mancinelli, N. J., & Fischer, K. M. (2017). The spatial sensitivity of Sp converted waves—Scattered wave kernels and their applications to receiver-function migration and inversion. *Geophysical Journal International*, *212*(3), 1722–1735. https://doi.org/10.1093/gji/ggx506
Mann, M. E., Abers, G. A., Daly, K., & Christensen, D. H. (2022). Subduction of an oceanic plateau across southcentral Alaska: Scattered-wave imaging. *Journal of Geophysical Research: Solid Earth*, *127*(1), e2021JB022697. https://doi.org/10.1029/2021jb022697
Martin-Short, R., Allen, R., Bastow, I. D., Porritt, R. W., & Miller, M. S. (2018). Seismic imaging of the Alaska subduction zone: Implications for slab geometry and volcanism. *Geochemistry, Geophysics, Geosystems*, *19*(11), 4541–4560. https://doi.org/10.1029/2018gc007962
McNamara, D. E., & Pasyanos, M. E. (2002). Seismological evidence for a sub-volcanic arc mantle wedge beneath the Denali volcanic gap, Alaska. *Geophysical Research Letters*, *29*(16), 61-1–61-4. https://doi.org/10.1029/2001GL014088
McPherson, A. M., Christensen, D. H., Abers, G. A., & Tape, C. (2020). Shear wave splitting and mantle flow beneath Alaska. *Journal of Geophysical Research: Solid Earth*, *123*(4), e2019JB018329. https://doi.org/10.1029/2019JB018329
Miller, E. L., & Hudson, T. L. (1991). Mid-Cretaceous extensional fragmentation of a Jurassic-Early Cretaceous compressional orogen, Alaska. *Tectonics*, *10*(4), 781–796. https://doi.org/10.1029/91tc00044
Miller, M. S., & Eaton, D. W. (2010). Formation of cratonic mantle keels by arc accretion: Evidence from *S* receiver functions. *Geophysical Research Letters*, *37*(18), L18305. https://doi.org/10.1029/2010gl044366
Miller, M. S., & Moresi, L. (2018). Mapping the Alaskan Moho. *Seismological Research Letters*, *89*(6), 1–7. https://doi.org/10.1785/0220180222
Miller, M. S., O'Driscoll, L. J., Butcher, A. J., & Thomas, C. (2015). Imaging Canary Island hotspot material beneath the lithosphere of Morocco and southern Spain. *Earth and Planetary Science Letters*, *431*, 186–194. https://doi.org/10.1016/j.epsl.2015.09.026

Miller, M. S., O'Driscoll, L. J., Porritt, R. W., & Roeske, S. M. (2018). Multiscale crustal architecture of Alaska inferred from P receiver functions. *Lithosphere*, *10*(2), 267–278. https://doi.org/10.1130/L701.1

Moll-Stalcup, E. J. (1994). Latest cretaceous and cenozoic magmatism in mainland Alaska. In G. Plafker & H. C. Berg (Eds.), *The geology of north America* (Vol. 1. pp. 589–619). GeologicalSociety of America.

Mukasa, S. B., Andronikov, A. V., & Hall, C. M. (2007). The $^{40}Ar/^{39}Ar$ chronology and eruption rates of Cenozoic volcanism in the eastern Bering Sea Volcanic Province, Alaska. *Journal of Geophysical Research*, *112*(B6), B06207. https://doi.org/10.1029/2006JB004452

Müller, R. D., Sdrolias, M., Gaina, C., & Roest, W. R. (2008). Age, spreading rates, and spreading asymmetry of the world's ocean crust. *Geochemistry, Geophysics, Geosystems*, *9*(4), Q04006. https://doi.org/10.1029/2007GC001743

Naif, S., Key, K., Constable, S., & Evans, R. L. (2013). Melt-rich channel observed at the lithosphere-asthenosphere boundary. *Nature*, *495*(7441), 356–359. https://doi.org/10.1038/nature11939

Nayak, A., Eberhart-Phillips, D., Ruppert, N. A., Fang, H., Moore, M. M., Tape, C., et al. (2020). 3D seismic velocity models for Alaska from joint tomographic inversion of body-wave and surface-wave data. *Seismological Research Letters*, *91*(6), 3106–3119. https://doi.org/10.1785/0220200214

Nye, C. J., Begét, J. E., Layer, P. W., Mangan, M. T., McConnell, V. S., McGimsey, R. G., et al. (2018). *Geochemistry of some quaternary lavas from the Aleutian Arc and Mt. Wrangell* (p. 29). Alaska Division of Geological and Geophysical Surveys. Raw Data File 2018-1. https://doi.org/10.14509/29843

O'Driscoll, L. J., & Miller, M. S. (2015). Lithospheric discontinuity structure in Alaska, thickness variations determined by Sp receiver functions. *Tectonics*, *34*(4), 694–714. https://doi.org/10.1002/2014TC003669

Plank, T., & Forsyth, D. W. (2016). Thermal structure and melting conditions in the mantle beneath the Basin and Range province from seismology and petrology. *Geochemistry, Geophysics, Geosystems*, *17*(4), 1312–1338. https://doi.org/10.1002/2015GC006205

Porritt, R. W., Miller, M. S., & Darbyshire, F. A. (2015). Lithospheric architecture beneath Hudson Bay. *Geochemistry, Geophysics, Geosystems*, *16*(7), 2262–2275. https://doi.org/10.1002/2015gc005845

Preece, S. J., & Hart, W. K. (2004). Geochemical variations in the 5 Ma Wrangell Volcanic Field, Alaska; implications for the magmatic and tectonic development of a complex continental arc system. *Tectonophysics*, *392*(1–4), 165–191. https://doi.org/10.1016/j.tecto.2004.04.011

Richter, D. H., Smith, J. G., Lanphere, M. A., Dalrymple, G. B., Reed, B. L., & Shew, N. (1990). Age and progression of volcanism, Wrangell Volcanic Field, Alaska. *Bulletin of Volcanology*, *53*(1), 29–44. https://doi.org/10.1007/BF00680318

Rondenay, S., Abers, G. A., & van Keken, P. E. (2008). Seismic imaging of subduction zone metamorphism. *Geology*, *36*(4), 275. https://doi.org/10.1130/G24112A.1

Rondenay, S., Montesi, L. G., & Abers, G. A. (2010). New geophysical insight into the origin of the Denali volcanic gap. *Geophysical Journal International*, *182*(2), 613–630. https://doi.org/10.1111/j.1365-246X.2010.04659.x

Roy, C., & Romanowicz, B. (2017). On the implications of a priori constraints in transdimensional Bayesian inversion for continental lithospheric layering. *Journal of Geophysical Research: Solid Earth*, *122*(12), 10118–10131. https://doi.org/10.1002/2017JB014968

Ruppert, N. A., & West, M. E. (2019). The impact of USArray on earthquake monitoring in Alaska. *Seismological Research Letters*, *91*(2A), 601–610. https://doi.org/10.1785/0220190227

Rychert, C. A., Harmon, N., & Tharimena, S. (2018a). Scattered wave imaging of the oceanic plate in Cascadia. *Science Advances*, *4*(2), eaao1908. https://doi.org/10.1126/sciadv.aao1908

Rychert, C. A., Harmon, N., & Tharimena, S. (2018b). Seismic imaging of the base of the ocean plates. In H. Yuan & B. A. Romanowicz (Eds.), *Lithospheric discontinuities, 239* (pp. 71–87). AGU Geophysical Monograph. https://doi.org/10.1002/9781119249740.ch4

Rychert, C. A., Laske, G., Harmon, N., & Shearer, P. M. (2013). Seismic imaging of melt in a displaced Hawaiian plume. *Nature Geoscience*, *6*(8), 657–660. https://doi.org/10.1038/ngeo1878

Rychert, C. A., Rondenay, S., & Fischer, K. M. (2007). *P*-to-*S* and *S*-to-*P* imaging of a sharp lithosphere-asthenosphere boundary beneath eastern North America. *Journal of Geophysical Research*, *112*(B8), B08314. https://doi.org/10.1029/2006jb004619

Schmandt, B., Lin, F.-C., & Karlstrom, K. E. (2015). Distinct crustal isostasy trends east and west of the Rocky Mountain Front. *Geophysical Research Letters*, *42*(23), 10290–10298. https://doi.org/10.1002/2015gl066593

Selway, K., O'Donnell, J. P., & Özaydin, S. (2019). Upper mantle melt distribution from petrologically constrained magnetotellurics. *Geochemistry, Geophysics, Geosystems*, *20*(7), 3328–3346. https://doi.org/10.1029/2019GC008227

Shen, W., & Ritzwoller, M. H. (2016). Crustal and uppermost mantle structure beneath the United States. *Journal of Geophysical Research: Solid Earth*, *121*(6), 4306–4342. https://doi.org/10.1002/2016jb012887

Shen, W., Ritzwoller, M. H., Schulte-Pelkum, V., & Lin, F.-C. (2013). Joint inversion of surface wave dispersion and receiver functions: A Bayesian Monte-Carlo approach. *Geophysical Journal International*, *192*(2), 807–836. https://doi.org/10.1093/gji/ggs050

Shen, W., Wiens, D. A., Anandakrishnan, S., Aster, R. C., Gerstoft, P., Bromirski, P. D., et al. (2018). The crust and upper mantle structure of central and West Antarctica from Bayesian inversion of Rayleigh wave and receiver functions. *Journal of Geophysical Research: Solid Earth*, *123*(9), 7824–7849. https://doi.org/10.1029/2017JB015346

Sifré, D., Gardés, E., Massuyeau, M., Hashim, L., Hier-Majumder, S., & Gaillard, F. (2014). Electrical conductivity during incipient melting in the oceanic low-velocity zone. *Nature*, *509*(7498), 81–85. https://doi.org/10.1038/nature13245

Soto Castaneda, R. A., Abers, G. A., Eilon, Z. C., & Christensen, D. H. (2021). Teleseismic attenuation, temperature, and melt of the upper mantle in the Alaska subduction zone. *Journal of Geophysical Research: Solid Earth*, *126*(7), e2021JB021653. https://doi.org/10.1029/2021JB021653

Stixrude, L., & Lithgow-Bertelloni, C. (2005). Mineralogy and elasticity of the oceanic upper mantle: Origin of the low-velocity zone. *Journal of Geophysical Research*, *110*(B3), B03204. https://doi.org/10.1029/2004jb002965

Syracuse, E. M., Abers, G. A., Fischer, K., MacKenzie, L., Rychert, C., Protti, M., et al. (2008). Seismic tomography and earthquake locations in the Nicaraguan and Costa Rican upper mantle. *Geochemistry, Geophysics, Geosystems*, *9*(7), Q07S08. https://doi.org/10.1029/2008GC001963

Tamura, Y. (2003). Some geochemical constraints on hot fingers in the mantle wedge: Evidence from NE Japan. *Geological Society, London, Special Publications*, *219*(1), 221–237. https://doi.org/10.1144/GSL.SP.2003.219.01.11

Trop, J. M., Benowitz, J. A., Kirby, C. S., & Brueseke, M. E. (2021). Geochronology of the Wrangell Arc: Spatial-temporal evolution of slab edge magmatism along a flat slab subduction-transform transition, Alaska-Yukon. *Geosphere*, *17*, 1–30. https://doi.org/10.1130/GES02417.1

Van Wijk, J. W., Lawrence, J. F., & Driscoll, N. W. (2008). Formation of the transantarctic mountains related to extension of the west Antarctic rift system. *Tectonophysics*, *458*(1–4), 117–126. https://doi.org/10.1016/j.tecto.2008.03.009

Veenstra, E., Christensen, D. H., Abers, G. A., & Ferris, A. (2006). Crustal thickness variation in south-central Alaska. *Geology*, *34*(9), 781–784. https://doi.org/10.1130/g22615.1

Venereau, C. M. A., Martin-Short, R., Bastow, I. D., Allen, R. M., & Kounoudis, R. (2019). The role of variable slab dip in driving mantle flow at the eastern edge of the Alaskan subduction margin: Insights from shear-wave splitting. *Geochemistry, Geophysics, Geosystems*, *20*, 2433–2448. https://doi.org/10.1029/2018gc008170

Wang, J., Takahashi, E., Xiong, X., Chen, L., Li, L., Suzuki, T., & Walter, M. J. (2020). The water-saturated solidus and second critical endpoint of peridotite: Implications for magma genesis within the mantle wedge. *Journal of Geophysical Research: Solid Earth*, *125*(8), e2020JB019452. https://doi.org/10.1029/2020JB019452

Wang, Y., & Tape, C. (2014). Seismic velocity structure and anisotropy of the Alaska subduction zone based on surface wave tomography. *Journal of Geophysical Research: Solid Earth*, *119*(12), 8845–8865. https://doi.org/10.1002/2014JB011438

Ward, K. M., & Lin, F.-C. (2018). Lithospheric structure across the Alaskan cordillera from the joint inversion of surface waves and receiver functions. *Journal of Geophysical Research: Solid Earth*, *123*(10), 8780–8797. https://doi.org/10.1029/2018JB015967

Wei, S. S., & Wiens, D. A. (2018). P-wave attenuation structure of the Lau back-arc basin and implications for mantle wedge processes. *Earth and Planetary Science Letters*, *502*, 187–199. https://doi.org/10.1016/j.epsl.2018.09.005

Wei, S. S., & Wiens, D. A. (2020). High bulk and shear attenuation due to partial melt in the Tonga-Lau back-arc mantle. *Journal of Geophysical Research: Solid Earth*, *125*(1), e2019JB017527. https://doi.org/10.1029/2019JB017527

Wu, Z., Chen, L., Talebian, M., Wang, X., Jiang, M., Ai, Y., et al. (2021). Lateral structural variation of the lithosphere-asthenosphere system in the northeastern to eastern Iranian plateau and its tectonic implications. *Journal of Geophysical Research: Solid Earth*, *126*(1), e2020JB020256. https://doi.org/10.1029/2020jb020256

Yamauchi, H., & Takei, Y. (2020). Application of a premelting model to the lithosphere-asthenosphere boundary. *Geochemistry, Geophysics, Geosystems*, *21*(11), e2020GC009338. https://doi.org/10.1029/2020gc009338

Yang, X., & Gao, H. (2020). Segmentation of the Aleutian-Alaska subduction zone revealed by full-wave ambient noise tomography: Implications for the along-strike variation of volcanism. *Journal of Geophysical Research: Solid Earth*, *125*(11), e2020JB019677. https://doi.org/10.1029/2020jb019677

Zhang, Y., Li, A., & Hu, H. (2019). Crustal structure in Alaska from receiver function analysis. *Geophysical Research Letters*, *46*(3), 1284–1292. https://doi.org/10.1029/2018GL081011